ELSEVIER

Localized deformation modes and non-Schmid effects in crystalline solids. Part II. deformation patterns

Ming Dao, Robert J. Asaro [*]

*Department of Applied Mechanics and Engineering Sciences, Mail Code 0411, University of California,
San Diego La Jolla, CA 92093, USA*

Abstract

A rate-dependent multiple slip model incorporating non-Schmid effects and thermal deformation, developed by Dao and Asaro (1993), is implemented into finite element codes to study deformation patterns before and after the shear band initiation in single crystals. Simulations using different hardening rates and different *non-Schmid effects* show that non-Schmid effects provide a consistent explanation for the formation of *coarse slip bands* (CSB), and that high hardening rates, typical of single crystals, can cause localization to not persist. Serrated flow is found accompanying the development of CSB's even with significant strain hardening. Elastic anisotropy has important influences on the onset of shear bands that form in single slip. Whether *macroscopic shear bands* (MSB) form first on directions that are close to what would be the primary slip plane or conjugate slip plane in a single crystal test, depends on the slip system geometry with respect to the loading orientation and the hardening function (self hardening and latent hardening). The transition from coarse slip bands to macroscopic shear bands is simulated and analyzed in detail, showing the importance of non-Schmid effects and the hardening function. Geometric effects, especially non-uniform lattice rotations, play important roles in the formation of both coarse slip bands and macroscopic shear bands. Consistency between the calculations and the theory predictions of the critical conditions of localization in Part I of this series (Dao and Asaro, 1996) as well as the existing experimental evidences are found.

1. Introduction

This paper represents the second part in a series concerned with non-Schmid effects and localized deformation in crystalline solids, and henceforth shall be referred to as Part II. In Part I (Dao and Asaro, 1996) we presented a rate independent version of a finite deformation slip theory incorporating non-Schmid effects and applied a general bifurcation analysis method studying critical conditions for lo-

calization. In Part II, herein, we will present a rate-dependent version of the finite deformation slip theory incorporating non-Schmid effects and use finite element calculations to examine the critical conditions for localization predicted in Part I. The simulation will also be used to study the development of localization and the transition of localization modes *after* the initiation of the localization process. Geometric effects such as non-uniform lattice rotations (*geometrical softening*) and orientation effects, along with material parameters like non-Schmid effects, self and latent hardening are the major focus in Part

[*] Corresponding author.

II. A detailed review of the literature relevant to this study can be found in Part I of this series (Dao and Asaro, 1996).

As mentioned in Part I (Dao and Asaro, 1996), it is important to understand that bifurcation analysis results can only serve as *necessary* conditions towards strain localization (see also Dao and Asaro, 1993), geometric effects like geometrical softening may sometimes play a decisive role in determining whether or not the shear bands will develop and the direction where the shear bands form.

Exploring the initiation and development of coarse slip bands (CSB) that are predicted in Part I (Dao and Asaro, 1996), studying the initiation direction and the development of the macroscopic shear bands (MSB) which are indicated possible in Part I, and providing a more comprehensive understanding of the transition from CSB's to MSB's are of particular interest here. Finite element computations of localized deformation pattern in polycrystals with non-Schmid effects were presented elsewhere (see Dao et al., 1996).

The plan of this paper is as follows. In the next section, Section 2.1, the rate-dependent constitutive theory is presented and Section 2.2 contains a detailed description of the finite element implementation used. Results are given in Section 3, where in Section 3.1 a brief description of the crystal model is given and the predictions in Part I (Dao and Asaro, 1996) are reviewed; in Section 3.2 results of localizations in single slip mode are given and the focus is on the initiation and development of CSB slip patterns; in Section 3.3 results of localizations in multiple slip mode are examined under both symmetric and non-symmetric loading conditions; and in Section 3.4 the transition from CSB's to MSB's is discussed in detail. Discussions follow in Section 4.

2. The theory and numerical considerations

Standard tensor notation is used throughout. Bold faced symbols are used to denote vectors and higher order tensors, the order of which will be clear in context. Products are indicated with dots, which denote summation over repeated Latin indices, and products containing no dots are dyadic products. Latin indices range from one to the number of spatial

dimensions, and repeated Latin indices are always summed. Inverses, transposes, and transposed inverses are denoted with a superscripted -1, T and $-T$, respectively and superposed dots indicate differentiation with respect to time t. For example,

$$A \cdot B = A_{ik}B_{kj}b_ib_j; \qquad A \times B = e_{ijk}A_jB_kb_i;$$

$$A:B = A_{ij}B_{ji}; \qquad AB = A_{ij}B_{kl}b_ib_jb_kb_l;$$

$$cd = c_id_jb_ib_j; \qquad B \cdot c = B_{ij}c_jb_i;$$

$$H:A = H_{ijkl}A_{lk}b_ib_j; \qquad \frac{\partial c}{\partial d} = \frac{\partial c_i}{\partial d_j}b_ib_j;$$

$$\dot{B} = \frac{\partial B_{ij}}{\partial t}b_ib_j,$$

where e_{ijk} is the permutation symbol, the basis b_i is Cartesian and independent of time, and greek indices are used to identify slip systems and range from one to $N =$ the number of slip systems. Summation over repeated nonparenthetical Greek indices is implied while repeated parenthetical Greek indices are not summed, e.g., $c_\alpha d_\alpha$ means $c_1d_1 + c_2d_2 + \cdots + c_Nd_N$ and $c_\alpha d_{(\alpha)}$ means either c_1d_1, c_2d_2, $\ldots$, or c_Nd_N.

2.1. The theory

The reference configuration is taken to be a defect-free perfect crystal, with an undeformed, stress free lattice along with its embedded material. The position of each material particle is given in this reference configuration by its position vector X. In this reference configuration, slip systems, designated and numbered by Greek letters are defined by the orthogonal pair of unit vectors (s_α, m_α), where s_α is parallel to the α slip direction in the reference configuration and m_α is normal to its slip plane. Note that such vectors are embedded in the crystal's lattice and will convect with it, i.e. they deform and rotate with the lattice in ways defined by models for plastic flow. The current configuration is defined as the elastically, thermally, and plastically deformed crystal, where the current position of each material particle is described by its current position vector x. The displacement vector, u, is given by $u = x - X$, and the deformation gradient F that maps the current configuration from the reference is given by
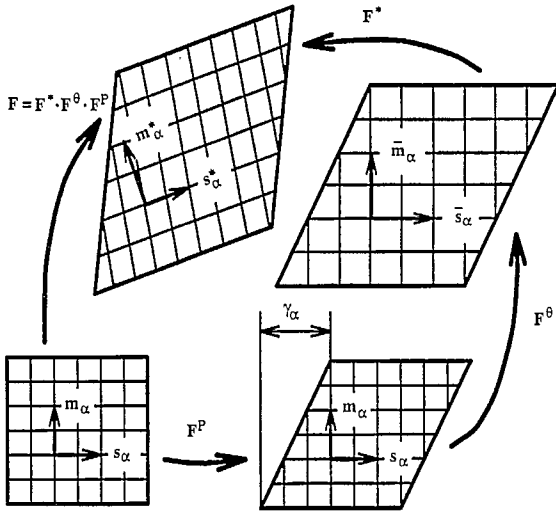
Fig. 1. Kinematic scheme of the deformation gradient decomposition.

$F = \partial x / \partial X = I + \partial u / \partial X$, where I is the second order identity tensor. In order to reach the current configuration from the reference, the plastic, thermal, and elastic parts of the total deformation are decomposed according to the kinematic scheme illustrated in Fig. 1.

One imagines that the material flows through the undeformed lattice by shear along the various slip systems of the crystal to reach the first intermediate configuration. The spatial velocity gradients of this plastic shear flow are written as

$$\dot{F}^P \cdot F^{P-1} = \dot{\gamma}_\alpha s_\alpha m_{(\alpha)}, \qquad (2.1)$$

where $\dot{\gamma}_\alpha$ is the shear rate on the α slip system and F^P is the plastic part of the deformation gradient. The value of F^P is given by the path dependent integration of Eq. (2.1).

From this plastically sheared state the second intermediate configuration is reached by imagining the crystal undergoing a general thermal deformation described by the thermal part of the deformation gradient, F^θ, where θ represents temperature. The spatial velocity gradients corresponding to this thermal deformation are written as

$$\dot{F}^\theta \cdot F^{\theta-1} = \dot{\theta}\alpha; \qquad \alpha = \alpha_{ij} a_i a_j, \qquad (2.2)$$

where α is a tensor whose components, α_{ij}, with respect to the time independent Cartesian base vectors, a_i, are the thermal expansion coefficients. The base vectors are aligned with the crystal lattice in the reference configuration in some standard way, e.g., in cubic crystals, it is most convenient to align the a_i base vectors with the cube axes, in which case α would be diagonal with all components equal.

The current configuration is reached by elastic deformation, along with possible rigid body rotation of the crystal lattice along with its embedded material. This part of the deformation is described by F^*, the lattice part of the deformation gradient. Hence according to the scheme described in Fig. 1, one obtains the deformation gradient decomposition,

$$F = F^* \cdot F^\theta \cdot F^P. \qquad (2.3)$$

Here, F is the deformation gradient describing the complete deformation. In reality the elastic distortion of the lattice, thermal deformation and plastic flow occur simultaneously, but it is clear that the current configuration of this model crystal can be reached by the above imagined steps of deformation. For concise further presentation of this development, we combine the various parts of the deformation gradient as follows,

$$\hat{F} = F^\theta \cdot F^P \quad \text{and} \quad \overline{F} = F^* \cdot F^\theta. \qquad (2.4)$$

The *loading parameter* for slip on slip system α, τ_α^D, is primarily the result of the so called *resolved shear stress* on that slip system along with what are generally thought to be relatively smaller contributions from components of stress other than the resolved shear stress. A particular form for the plastic flow law is described below. The generalized stress which acts to load a slip system is given as

$$\tau_\alpha^D = \tau_\alpha + \eta_\alpha : \tau = m_\alpha^* \cdot \tau \cdot s_\alpha^* + \eta_\alpha : \tau, \qquad (2.5a)$$

$$s_\alpha^* = \overline{F} \cdot s_\alpha; \qquad m_\alpha^* = m_\alpha \cdot \overline{F}^{-1};$$

$$z_\alpha^* = s_\alpha^* \times m_\alpha^*, \qquad (2.5b)$$

$$\tau = J\sigma, \qquad (2.5c)$$

where $J = \det\{F\}$ is the Jacobian, τ is the Kirchhoff stress tensor, σ is the Cauchy stress tensor, s_α^* is along the α slip direction in the current configuration, m_α^* is normal to the α slip plane, z_α^* is normal

to both s_α^* and m_α^*, and $\boldsymbol{\eta}_\alpha$ is the tensor of non-Schmid effects for slip system α which, when aligned with s_α^*, m_α^* and z_α^*, takes the simple form,

$$\boldsymbol{\eta} = \begin{pmatrix} \eta_{ss} & 0 & \eta_{sz} \\ 0 & \eta_{mm} & \eta_{mz} \\ \eta_{sz} & \eta_{mz} & \eta_{zz} \end{pmatrix}. \qquad (2.6)$$

The kinetic description of plasticity on each slip system is cast in terms of the loading parameter τ_α^D and the slip rate on that system as

$$\dot{\gamma}_\alpha = \dot{a}\,\mathrm{sgn}\{\tau_\alpha\}\left\{\left|\frac{\tau_{(\alpha)}^D}{g_{(\alpha)}}\right|\right\}^{1/m}, \qquad (2.7)$$

where τ_α is the current value of the resolved shear stress, τ_α^D is the loading parameter for slip as defined in Eq. (2.5), and $g_\alpha > 0$ is the current value of the *slip system hardness*. In Eq. (2.7), m is the material rate sensitivity exponent (which will, in the examples described herein, be taken the same for each slip system), and $\dot{a}$ is the reference shear rate. The slip system hardness g_α is obtained by the path dependent integration of the evolution equation

$$\dot{g}_\alpha = h_{\alpha\beta}(\gamma_\alpha)|\dot{\gamma}_\beta| + g_\alpha^\theta\dot{\theta}, \quad \gamma_a = \int_0^t \sum_\alpha |\dot{\gamma}_\alpha|\,\mathrm{d}t,$$

$$(2.8)$$

where $h_{\alpha\beta}$ is a matrix of (positive) hardening moduli, g_α^θ is the rate of change of slip system hardness with respect to temperature alone, and γ_a is the accumulated sum of slips. The initial condition for this evolution are given by $g_\alpha(\gamma_a = 0,\ \theta = \theta_0) = g_0(\theta_0)$ where θ_0 is an initial temperature.

The single crystal's constitutive description is completed with a specification of its elasticity, which is expressed in terms of S^*, the lattice-based second Piola-Kirchhoff stress, and E^*, the Green strain of the lattice. These quantities are written as

$$E^* = \tfrac{1}{2}(F^{*T}\cdot F^* - I);$$
$$S^* = F^{*-1}\cdot \tau \cdot F^{*-T}, \qquad (2.9)$$

where I is the second order identity tensor. Let $\Phi = \Phi(E_{ij}^*)$ be the Helmholtz free energy of the lattice per unit reference volume, then

$$S_{ij}^* = \frac{\partial \Phi}{\partial E_{ij}^*}; \qquad S^* = S_{ij}^* a_i a_j; \qquad E^* = E_{ij}^* a_i a_j,$$

$$(2.10)$$

where the time-independent Cartesian base vectors a_i are aligned with the crystal lattice in the reference configuration in some standard way. Differentiation of the first of Eq. (2.10) with respect to time gives the rate form

$$\dot{S}^* = K:\dot{E}^*; \qquad K = K_{ijkl}a_i a_j a_k a_l;$$

$$K_{ijkl} = \frac{\partial^2 \Phi}{\partial E_{ij}^* \partial E_{kl}^*}. \qquad (2.11)$$

The final constitutive theory is expressed in terms of the second Piola-Kirchhoff stress, $S = F^{-1}\cdot \tau \cdot F^{-T}$, and the Green (or Lagrangian) strain, $E = \tfrac{1}{2}(F^T\cdot F - I)$. Straightforward manipulation of the above equations give the rate form of the governing constitutive equation, viz.

$$\dot{S} = L:\dot{E} - \dot{\gamma}_\alpha X_\alpha - \dot{\theta}Y, \qquad (2.12)$$

where

$$L_{ijrn} = \hat{F}_{ik}^{-1}\hat{F}_{jl}^{-1}K_{klpq}\hat{F}_{rp}^{-1}\hat{F}_{nq}^{-1};$$

$$L = L_{ijkl}a_i a_j a_k a_l; \qquad \hat{F}^{-1} = \hat{F}_{ij}^{-1}a_i a_j \qquad (2.13)$$

and

$$X_\alpha = \hat{F}^{-1}\cdot\{K:A_\alpha + 2H_\alpha\}\cdot\hat{F}^{-T};$$

$$Y = \hat{F}^{-1}\cdot\{K:B + 2Q\}\cdot\hat{F}^{-T};$$

$$A_\alpha = \mathrm{sym}\{F^{*T}\cdot F^*\cdot F^0\cdot\{s_\alpha m_{(\alpha)}\}\cdot F^{0-1}\};$$

$$H_\alpha = \mathrm{sym}\{F^\theta\cdot\{s_\alpha m_{(\alpha)}\}\cdot F^{0-1}\cdot S^*\};$$

$$B = \mathrm{sym}\{F^{*T}\cdot F^*\cdot\alpha\}; \qquad Q = \mathrm{sym}\{\alpha\cdot S^*\}.$$

$$(2.14)$$

Given the current state $s = \{S^*,\ E^*;\ F^P,\ F^\theta,\ g_\alpha\}$, which is described by both state and internal variables, one can obtain the slip rates, $\dot{\gamma}_\alpha$, unambiguously from Eq. (2.7). The state s also unambiguously specifies the tensors L, $\dot{\gamma}_\alpha X_\alpha$ and Y, so that Eq. (2.12) provides a linear relation between $\dot{S}$ and $\dot{E}$. Using the linear elasticities ensures that K_{ijkl} is invertible, since plasticity here is still taken as incompressible we have $\det\{F^P\} = 1$ and for finite thermal expansion coefficients it can be shown that $\det\{F^\theta\} > 0$ so that L is invertible. Therefore, the relation between $\dot{S}$ and $\dot{E}$ is always invertible ensur-
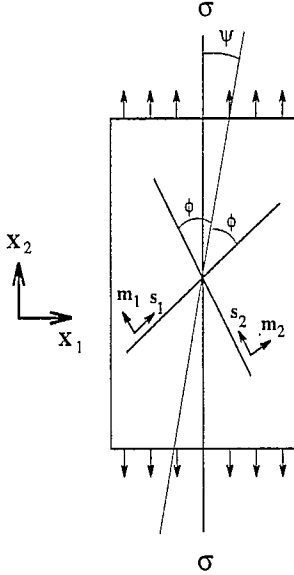
Fig. 2. Plane strain primary-conjugate double slip geometry, where two slip systems tilted from the double symmetric slip position for ψ degrees and both the slip vectors s_1, s_2 and slip plane normals m_1, m_2 are in the drawing's plane.

ing the uniqueness of solution to mixed boundary value problem in this study.

2.2. Numerical implementation

The rate constitutive equations, notably Eq. (2.12), are implemented by the one step, explicit rate tangent method introduced by Peirce et al. (1983). In this method, an estimation is made for the change in shear rates, $\dot{\gamma}_\alpha$, within the current time increment. An algorithm was also proposed by Rashid and Nemat-Nasser (1990), Rashid and Nemat-Nasser (1992) for a rate-dependent double slip single crystal model, which is suitable for implementation in an explicit finite element code such as PRONTO2D and appropriate for high strain rate problems.

Although the theory in Section 2.1 is developed for a general three dimensional slip geometry, we use the planar primary-conjugate double slip geometry as shown in Fig. 2, where the two slip systems are tilted from the double symmetric slip position for ψ degrees ($\psi = 0$ represents double symmetric slip) and both slip vectors, s_1 and s_2, and slip plane normals, m_1 and m_2, are in the drawing's plane. For the actual crystals, this is not strictly true though the

deformation patterns will be quite similar for the real crystals and the idealized ones studied herein.

Within two dimensional geometry, we rewrite Eq. (2.6a) to be

$$\tau_\alpha^D = m_\alpha^* \cdot \tau \cdot s_\alpha^* + \eta_{ss} s_\alpha^* \cdot \tau \cdot s_\alpha^* + \eta_{mm} m_\alpha^* \cdot \tau \cdot m_\alpha^*$$
$$= \tau_\alpha + \eta_{ss}\tau_\alpha^{ss} + \eta_{mm}\tau_\alpha^{mm}, \qquad (2.15)$$

where

$$\tau_\alpha = m_\alpha^* \cdot \tau \cdot s_\alpha^*; \qquad \tau_\alpha^{ss} = s_\alpha^* \cdot \tau \cdot s_\alpha^*;$$
$$\tau_\alpha^{mm} = m_\alpha^* \cdot \tau \cdot m_\alpha^*. \qquad (2.16)$$

Assuming non-Schmid tensor $\eta = \eta(\theta)$, differentiate Eq. (2.15) with respect of time we get

$$\dot{\tau}_\alpha^D = \dot{\tau}_\alpha + \eta_{ss}\dot{\tau}_\alpha^{ss} + \eta_{mm}\dot{\tau}_\alpha^{mm} + M\dot{\theta}, \qquad (2.17)$$

where

$$M = \frac{\partial \eta_{ss}}{\partial \theta}\tau_\alpha^{ss} + \frac{\partial \eta_{mm}}{\partial \theta}\tau_\alpha^{mm}. \qquad (2.18)$$

The slip increment on slip system α for the time increment, Δt, beginning at time t is defined by

$$\Delta\gamma_\alpha = \dot{\gamma}_\alpha^{t+\Delta t} - \dot{\gamma}_\alpha^t, \qquad (2.19)$$

where $(\cdot)^t$ and $(\cdot)^{t+\Delta t}$ indicate $(\cdot)$ evaluated at time t and $t+\Delta t$ respectively. A linear interpolation is applied within the time increment to obtain

$$\Delta\gamma_\alpha = \left[(1-\Theta)\dot{\gamma}_\alpha^t + \Theta\dot{\gamma}_\alpha^{t+\Delta t}\right]. \qquad (2.20)$$

The parameter Θ ranges from 0 to 1; $\Theta = 0$ corresponds to simple Euler integration scheme. To approximate the last term in Eq. (2.20) a Taylor expansion of the rate relation given by Eq. (2.7) to the first order in incremental quantities is employed,

$$\dot{\gamma}_\alpha^{t+\Delta t} = \dot{\gamma}_\alpha^t + \left.\frac{\partial \dot{\gamma}_{(\alpha)}}{\partial \tau_{(\alpha)}^D}\right|_t \Delta\tau_\alpha^D + \left.\frac{\partial \dot{\gamma}_{(\alpha)}}{\partial g_{(\alpha)}}\right|_t \Delta g_\alpha$$

$$= \text{sgn}\{\tau_\alpha\}\left\{\left(\left|\frac{\tau_{(\alpha)}^D}{g_{(\alpha)}}\right|\right)^{1/m}\right\}$$

$$\times \left\{1 + \frac{1}{m}\left(\frac{\Delta\tau_{(\alpha)}^D}{\tau_{(\alpha)}^D} - \frac{\Delta g_{(\alpha)}}{g_{(\alpha)}}\right)\right\}, \qquad (2.21)$$

where $\Delta\tau_\alpha^D = \dot{\tau}_\alpha^D\Delta t$ and $\Delta g_\alpha = \dot{g}_\alpha\Delta t$. An expression relating $\dot{\tau}_\alpha^D$ and $\dot{\gamma}_\alpha$ is determined as follows. Manipulating Eq. (2.16) yields

$$\tau_\alpha = s_\alpha \cdot \overline{C} \cdot \overline{S} \cdot m_{(\alpha)}; \qquad (2.22a)$$

$$\tau_\alpha^{ss} = \left(\overline{C} \cdot s_\alpha\right) \cdot \overline{S} \cdot \left(\overline{C} \cdot s_{(\alpha)}\right); \tag{2.22b}$$

$$\tau_\alpha^{mm} = m_\alpha \cdot \overline{S} \cdot m_\alpha, \tag{2.22c}$$

where $\overline{C} = \overline{F}^T \cdot \overline{F}$ is the right Cauchy–Green strain of the thermal and elastic deformations and $\overline{S} = \overline{F}^{-1} \cdot \tau \cdot \overline{F}^{-T}$ is the second Piola–Kirchhoff stress on the first intermediate configuration. Differentiating Eqs. (2.22a–c) with respect to time and using Eqs. (2.4), (2.9), (2.11), (2.14) and (2.17) we obtain after manipulation

$$\dot{\tau}_\alpha^D = X_\alpha^D : \dot{E} - R_\alpha^D : \left[\dot{\gamma}_\beta A_\beta + \dot{\theta} B\right] + G_\alpha^D + M\dot{\theta}, \tag{2.23}$$

where

$$X_\alpha^D = \hat{F}^{-1} \cdot R_\alpha^D \cdot \hat{F}^{-T};$$

$$R_\alpha^D = R_\alpha + \eta_{ss} R_\alpha^{ss} + \eta_{mm} R_\alpha^{mm};$$

$$G_\alpha^D = G_\alpha + \eta_{ss} G_\alpha^{ss} + \eta_{mm} G_\alpha^{mm}, \tag{2.24}$$

and where

$$R_\alpha = K : A_\alpha + 2 H_\alpha;$$

$$R_\alpha^{ss} = K : \left[C^* \cdot F^\theta \cdot (s_\alpha s_{(\alpha)}) \cdot F^{\theta T} \cdot C^*\right]$$
$$+ 4 \operatorname{sym}\left[F^\theta \cdot (s_\alpha s_{(\alpha)}) \cdot F^{\theta T} \cdot C^* \cdot S^*\right];$$

$$R_\alpha^{mm} = K : \left[F^{\theta-T} \cdot (m_\alpha m_{(\alpha)}) \cdot F^{\theta-1}\right];$$

$$G_\alpha = \operatorname{sym}\left\{\dot{F}^\theta \cdot (s_\alpha m_{(\alpha)}) \cdot F^{\theta-1} + F^\theta \cdot (s_\alpha m_{(\alpha)})\right.$$
$$\left. \cdot F^{\theta-1}\right\} : S^* \cdot C^*;$$

$$G_\alpha^{ss} = 2 s_\alpha \cdot \dot{F}^{\theta T} \cdot C^* \cdot S^* \cdot C^* \cdot F^\theta \cdot s_{(\alpha)};$$

$$G_\alpha^{mm} = 2 m_\alpha \cdot \dot{F}^{\theta-1} \cdot S^* \cdot F^{\theta-T} \cdot m_{(\alpha)}. \tag{2.25}$$

Using Eq. (2.23) and the first of Eq. (2.8) (which gives $\dot{g}_\alpha$ in terms of $\dot{\gamma}_\alpha$) in Eqs. (2.21) and (2.20) one obtains after manipulation

$$N_{\alpha\beta} \Delta\gamma_\beta$$
$$= \dot{\gamma}_\alpha^t \Delta t \left[1 + \frac{\Theta \Delta t}{m} \left\{\frac{1}{\tau_{(\alpha)}^D} \left(X_{(\alpha)}^D : \dot{E} - R_{(\alpha)}^D : \dot{\theta} B\right.\right.\right.$$
$$\left.\left.\left. + G_{(\alpha)}^D\right) - \left(\frac{g_{(\alpha)}^\theta}{g_{(\alpha)}} - \frac{M}{\tau_{(\alpha)}^D}\right) \dot{\theta}\right\}\right], \tag{2.26}$$

where

$$N_{\alpha\beta} = \delta_{\alpha\beta} + \frac{\Theta \dot{\gamma}_\alpha^t \Delta t}{m}$$
$$\times \left\{\frac{R_{(\alpha)}^D : A_\beta}{\tau_{(\alpha)}^D} + \operatorname{sgn}\{\tau_\beta\} \frac{h_{(\alpha)(\beta)}}{g_{(\alpha)}}\right\}. \tag{2.27}$$

Note that for fixed Θ and m, $N_{\alpha\beta}$ is invertible for sufficiently small Δt. Also in general, $N_{\alpha\beta} \neq N_{\alpha\beta}$. Inverting Eq. (2.26) and dividing by Δt yields

$$\dot{\gamma}_\alpha^d = \frac{\Delta\gamma_\alpha}{\Delta t} = \dot{f}_\alpha + F_\alpha : \dot{E}, \tag{2.28}$$

where

$$\dot{f}_\alpha = N_{\alpha\beta}^{-1} \dot{\gamma}_\beta^t \left[1 + \frac{\Theta \Delta t}{m} \left\{\frac{1}{\tau_{(\beta)}^D} \left(G_{(\beta)}^D - R_{(\beta)}^D : \dot{\theta} B\right)\right.\right.$$
$$\left.\left. - \left(\frac{g_{(\beta)}^\theta}{g_{(\beta)}} - \frac{M}{\tau_{(\beta)}^D}\right) \dot{\theta}\right\}\right]; \tag{2.29}$$

$$F_\alpha = N_{\alpha\beta}^{-1} \frac{\Theta \dot{\gamma}_\beta^t \Delta t}{m \tau_{(\beta)}^D} X_{(\beta)}^D \tag{2.30}$$

and where $(\dot{\ })^d$ indicates the time discrete rate of $(\cdot)$.

The temperature change for the increment is defined by

$$\Delta\theta = \theta^{t+\Delta t} - \theta^t. \tag{2.31}$$

As for the slip increment a linear interpolation is employed within the time increment to obtain

$$\Delta\theta = \left[(1 - \Theta)\dot{\theta}^t + \Theta \dot{\theta}^{t+\Delta t}\right] \Delta t. \tag{2.32}$$

$\dot{\theta}$ is expanded in a Taylor series about time t to first order in Δt. The substitution of this expansion into Eq. (2.32) and division by Δt results in a time discrete rate of temperature change of the form

$$\dot{\theta}^d = \frac{\Delta\theta}{\Delta t} = \dot{\theta}^t + \Theta \ddot{\theta}^t \Delta t. \tag{2.33}$$

Identifying $\dot{\theta}$ with its time discrete counterpart for the increment, $\dot{\theta}^d$, allows both $\dot{f}_\alpha$ and F_α, and hence $\dot{\gamma}_\alpha^d$, to be determined from the state at time t. If further, one identifies $\dot{\gamma}_\alpha$ with its time discrete counterpart for the increment, $\dot{\gamma}_\alpha^d$, the time discrete ver-

sion of the governing rate relations, Eq. (2.12), can be written as

$$\dot{S}^d = L^{\tan} : \dot{E}^d - \dot{X}^{\tan}, \qquad (2.34)$$

where

$$L^{\tan} = L - X_\alpha F_\alpha; \qquad \dot{X}^{\tan} = \dot{f}_\alpha X_\alpha - \dot{\theta}^d Y. \qquad (2.35)$$

L^{tan} and $\dot{X}^{tan}$ are determined explicitly from the state at time t.

Boundary value problems in this theory can be solved using the finite element method. The above numerical integration scheme is implemented in a finite element context via the principle of virtual work, as is outlined in Dève et al. (1988), Harren and Asaro (1989) and McHugh et al. (1993). In order to enforce equilibrium at the end of the time step, the principle of virtual work is written as

$$\int_V n^{t+\Delta t} : \delta F \, dV = \int_S t^{t+\Delta t} \cdot \delta u \, dS, \qquad (2.36)$$

where the body force has been ignored. The integration is over the reference configuration V, whose surface is S. Also, $t = N \cdot n$ is the nominal traction vector (N is the outward unit normal to S), $n = F^{-1} \cdot \tau = S \cdot F^T$ is the nominal stress and δu is an admissible variational displacement field that is compatible with the variational deformation gradient field, δF. To obtain the evolution of the solution through time, the explicit difference relation $n^{t+\Delta t} = n^t + \dot{n}^d \Delta t$ is substituted into Eq. (2.36) as are the relations

$$n^t : \delta F = S^t : \delta E; \qquad \delta E = \text{sym}\left\{ (F^t)^T \cdot \delta F \right\};$$

$$\dot{n}^d : \delta F = \dot{S}^d : \delta E + \left\{ S^t \cdot (\dot{F}^d)^T \right\} : \delta F. \qquad (2.37)$$

The governing time discrete rate form, Eq. (2.34), is substituted into the result yielding

$$\int_V \left[\delta E : L^{\tan} : \dot{E}^d + \left\{ S^t \cdot (\dot{F}^d)^T \right\} : \delta F \right] dV$$

$$= \int_V \left\{ \dot{X}^{\tan} - \frac{1}{\Delta t} S^t \right\} : \delta E \, dV + \frac{1}{\Delta t} \int_S t^{t+\Delta t} \cdot \delta u \, dS. \qquad (2.38)$$

This time-discrete variational equation is then written in Cartesian indicial form on the reference orthonormal base vectors e_i and then the usual finite

element interpolation and gradient operators are introduced to obtain a linear system of equations. After applying the appropriate rate boundary conditions the equations are solved for the time discrete nodal velocities which yield $\dot{F}^d$, $\dot{E}^d$ and the incremental displacement field.

In updating the state from time t to time $t + \Delta t$ one begins by calculating the slip increments using Eq. (2.28). Next, the increments in g_α are obtained from Eq. (2.8). The increment in the stress state is obtained from Eq. (2.34) using the now known $\dot{E}^d$. Once the incremental quantities that depend on the geometry at time t have been found, the geometry itself can be updated. The new displacements give the new deformation gradient, F. The increments in F^P and F^θ are obtained using Eqs. (2.1) and (2.2), respectively. The new F^* is then given by $F^* = \hat{F}^{-1}$. The specification of the new s_α^*, m_α^* and τ_α^D completes the update, allowing one to proceed to the next time increment. In choosing stable time steps for the integration algorithm the scheme presented in Harren et al. (1988) was used.

In this paper, we simulate only deformations performed at a constant temperature. Specific reference to temperature will be omitted in later sections.

3. Results

3.1. Model perspectives

In a two dimensional geometry as described in Fig. 2, the only non-Schmid factors are η_{ss} and η_{mm} ($\eta_{ss} = \eta_{mm} = 0$ corresponds to Schmid's rule) and this geometry is actually the type I double slip geometry discussed in Part I of this series (Dao and Asaro, 1996), assuming both primary and conjugate slip systems are active. Noting that the primary slip system will be activated first for $\psi \neq 0°$, the deformation is in single slip at first and then gradually transfer to a double slip mode. We thus will use this geometry to explore the localization process in single slip and multiple slip mode.

Since there are systematic experimental documentations about Al–Cu single crystals (see Harren et al., 1988; Chang and Asaro, 1981; Chang, 1979), Al–Cu single crystal material constants are used in

our computations. Here we apply the general method used in Part I (Dao and Asaro, 1996) to identify critical localization conditions under single slip as well as multiple slip mode.

3.1.1. Critical localization conditions in single slip mode

If we take, for example, the critical resolved shear stress at initial yielding $g_0 \approx 46$ MPa for Al–Cu single crystal, the elastic shear moduli $G \approx 26$ GPa $= 570 g_0$ and Poisson's ratio $\nu = 0.33$, and assume that $\eta_{ss} = 0.08$, then the critical hardening rate h_{cr} for single slip shear bands is given as $h_{cr} = 2.736 g_0$ $= 126$ MPa and the misorientation of the bands will be about 2.3°. When $\eta_{ss} = 0.04$, h_{cr} will be $0.684 g_0$ with a band misorientation of 1.1°; and when Schmid's rule holds, $h_{cr} \leq 0$ with the band's misorientation being 0°. For details, refer to Part I (Dao and Asaro, 1996; Asaro and Rice, 1977). Elastic anisotropy is found to have an important influence towards the critical localization conditions (Dao and Asaro, 1996).

3.1.2. Critical localization conditions in multiple slip mode

For the case of double symmetric slip, taking $\phi = 30°$, when $\eta_{ss} = 0.08$ the critical hardening rate h_{cr} is calculated as $h_{cr} = 0.071 \sigma_{22}$ with the band misorientation of 8.5°, where σ_{22} is the tensile stress. If we take a reasonable number for the saturation value of the resolved shear stress on one slip system to be $1.8 g_0$ which gives $\sigma_{22} = 1.8 g_0 \sin \phi \cos \phi = 4.156 g_0$, then for $\eta_{ss} = 0.08$ we have $h_{cr} = 0.295 g_0$. Similarly, when $\eta_{ss} = 0.04$ we have $h_{cr} = 0.060 \sigma_{22}$

$= 0.249 g_0$ with bands misorientation of 7.9°; and when Schmid's rule holds, we have $h_{cr} = 0.050 \sigma_{22}$ $= 0.208 g_0$ with bands misorientation of 7.4°.

If the slip geometry is not symmetric, the conjugate slip system is favored by our bifurcation analyses. Elastic anisotropy is found to have negligible effects towards the critical localization conditions in this case. It was also speculated in Part I (Dao and Asaro, 1996) that the latent hardening ratio would have an important influence towards the initiation as well as the development of the localized deformation mode, i.e. for $q < 1$ double slip mode may begin before the symmetric boundary is reached and shear bands will favor conjugate slip system, while for $q > 1$ double slip mode may begin only after some overshooting (a conjugate to primary switch happens here) and shear bands will favor the originally primary slip system (but actually the currently conjugate slip system).

3.1.3. Summary of theoretical predictions

Some results of critical localization conditions are listed in Table 1 for both single slip and multiple slip deformation mode (type I geometry) under the planar slip geometry. For this plane strain geometry (Fig. 2), it is obvious that when $\eta_{ss} \neq 0$ the single slip bands can form under high strain hardening rates and the single slip bands are very close to the slip plane (less than 2.3°) while the bands forming under conditions of double slip are 7°–9° misoriented. The single slip shear bands with $\eta_{ss} \neq 0$ can form at much higher hardening rates than the double slip bands (type I); and if the Schmid rule holds, single slip shear bands are not possible unless there is perfect

Table 1
Selected results of shear bands for different deformation modes and slip geometry

	Deformation mode	h_{cr}	Misorientation	Influence of elastic anisotropy	Influence of nonsymmetric loading
Schmid's rule	single slip	0	0°	—	—
	double slip (type I)	$0.208 g_0$	7.4°	no	favor conjugate
$\eta_{ss} = 0.04$–0.08	single slip	0.684–$2.736 g_0$	1.1°–2.3°	yes	—
	double slip (type I)	0.249–$0.295 g_0$	7.9°–8.5°	no	favor conjugate
$\eta_{mm} = 0.04$–0.08	single slip	0	0°	—	—
	double slip (type I)	0.241–$0.279 g_0$	7.9°–8.6°	no	favor conjugate

plasticity or strain softening, while at the same time, double slip shear bands (type I) can still form under significant positive strain hardening.

3.2. Shear bands under single slip mode

From the bifurcation analyses (Dao and Asaro, 1996) which are summarized in Section 3.1 for the slip geometry we are using here, it is obvious that when $\eta_{ss} \neq 0$ there can be single slip bands forming at quite high hardening rates, while there will not be any single slip bands under positive strain hardening when $\eta_{ss} = 0$, $\eta_{mm}0$ or when Schmid's rule holds. It is also speculated that, if the strain hardening is significant, shear bands will not persist at the same location, but instead bands will tend to be coarsely spread along the active gage length of the crystals (Price and Kelly, 1964; Dao and Asaro, 1994, Dao and Asaro, 1996). The misorientation between the single slip shear bands and the active slip system should be very small, and elastic anisotropy should play an important role. To verify those theoretical predictions, we will design a *computational experiment* as follows: (1) imagine a defect free virgin crystal (except very small geometric imperfections), the slip system geometry is as shown in Fig. 2 with $\phi = 30°$ and $\psi = 10°$; (2) let the self hardening rate $h_{11} = h_{22} = h$ be fixed from 0 to 3% macroscopic engineering strain for this 'model crystal'; (3) latent hardening ratio $q = 1$; and (4) the finite element
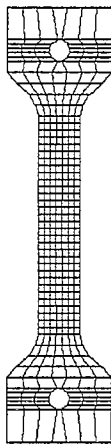

Fig. 3. Finite element mesh used in calculations for single slip shear bands. The mesh is built with two grips, where the gage section is L_0 long and b_0 wide with 31×7 elements.

mesh is built with two grips (see Fig. 3), with the small initial geometric imperfection taken as $\Delta b_0 = 0.006 b_0 \cos(2\pi x^2/L_0)$, where the gage section is L_0 long and b_0 wide (31×7 elements). One notices that this tensile 'specimen' is oriented for single slip, at least initially.

3.2.1. Influences of strain hardening and the non-Schmid effects

When the elasticity is isotropic, the critical hardening rate for localization is of the form

$$h_{cr} = h_{cr}(\eta_{ss}, G) \propto \eta_{ss}^2 G$$

for the two dimensional geometry, where G is the elastic shear moduli.

3.2.1.1. Effect of strain hardening. If we take, for example, the critical resolved shear stress at initial yielding $g_0 \approx 46$ MPa for Al–Cu single crystal, the elastic shear moduli $G \approx 26$ GPa $= 570 g_0$ and Poisson's ratio $v = 0.33$, then the critical hardening rate for the onset of single slip shear bands will be given as

$$h_{cr}^{iso} = h_{cr}^{iso}(\eta_{ss} = 0.08) = 2.736 g_0.$$

In what follows the material rate sensitivity exponent m is taken as 0.005 for all cases.

Fig. 4a–f show maps of the accumulated sum of slips at 3% engineering strain under different hardening rates: (a) $h = 1.05 h_{cr}^{iso} = 2.8728 g_0$, (b) $h = 0.8 h_{cr}^{iso} = 2.1888 g_0$, (c) $h = 0.5 h_{cr}^{iso} = 1.368 g_0$, (d) $h = 0.3 h_{cr}^{iso} = 0.8208 g_0$, (e) $h = 0.04 h_{cr}^{iso} = 0.10944 g_0$, and (f) $h = 0$, respectively. It is very clear that (1) when $h > h_{cr}$ (i.e. Fig. 4a), the deformation is essentially uniform, no localization observed in the gage section; (2) when h is significant but $h < h_{cr}$ (i.e. Fig. 4b–d), CSB localization pattern is the major deformation mode; where localization develops faster and deeper as h drops; (3) when h is very low but still positive (i.e. Fig. 4e), the CSB's tend to develop close to each other — or in another word clustering; (4) when $h = 0$ (i.e. Fig. 4f), the shear band will persist at the same location, no CSB pattern is forming; and (5) the peak strains accumulated in those CSB's go higher as the hardening rate decreases (see Fig. 4b–f). In Fig. 4b–f, all shear bands are closely aligned with the active slip system. Fig. 5a–c show maps of shear rate on slip system 1

at 1%, 2% and 3% engineering strain respectively; the hardening rate was taken as $h = 0.5h_{cr}^{iso}$. Noting that in Fig. 5a–c, the most active slip bands switch their positions instead of persisting at the same location as the macroscopic strain increases. The same sort of 'switching' was also found in cases where
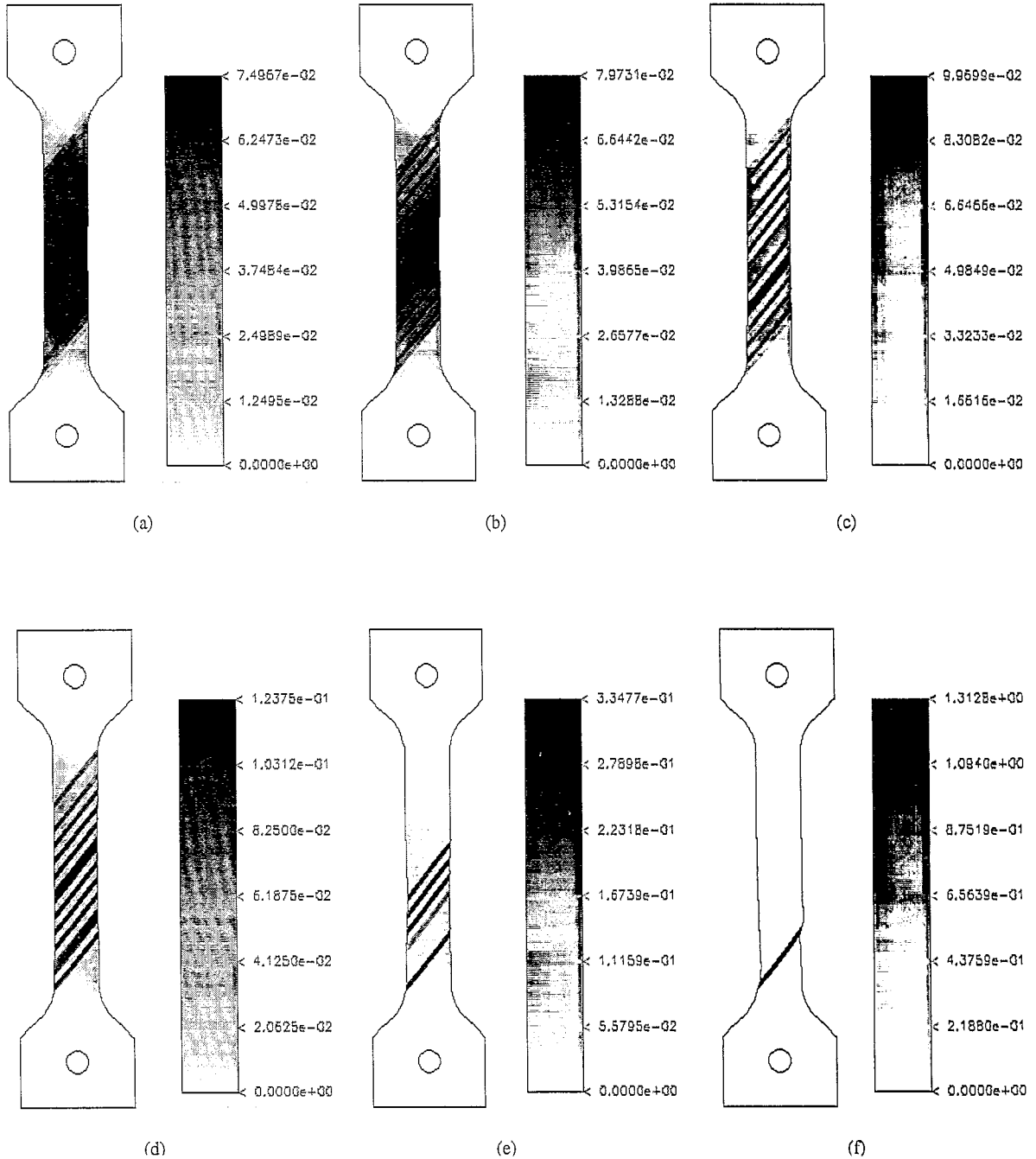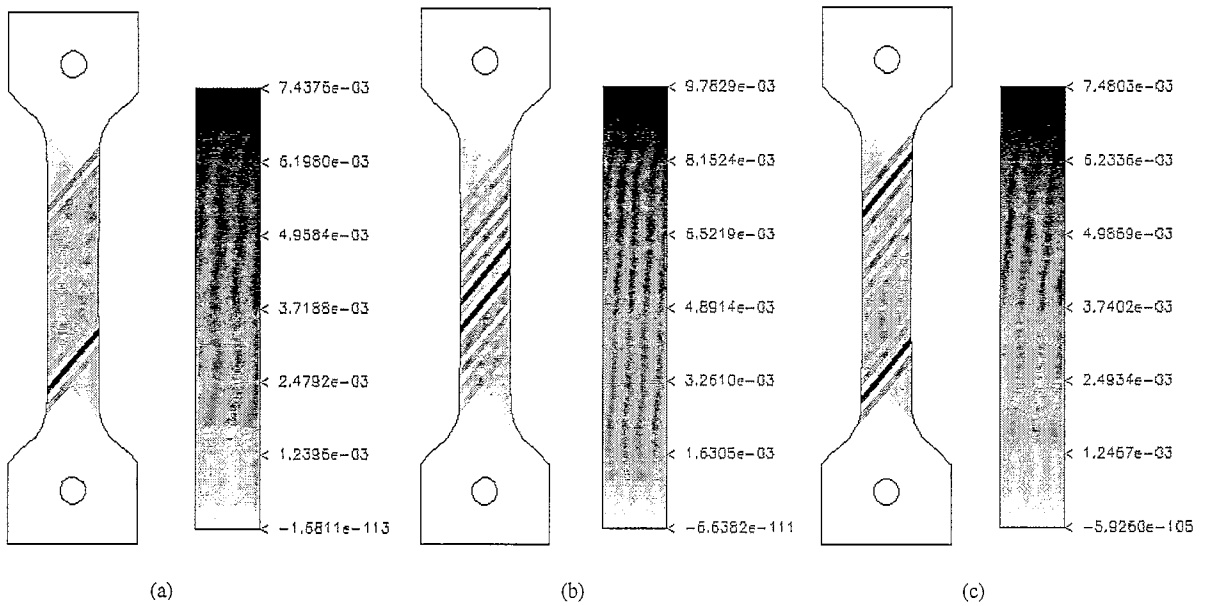

Fig. 4. Maps of the accumulated sum of slips at 3% engineering strain under different hardening rates: (a) $h = 1.05h_{cr}^{iso} = 2.8728\,g_0$, (b) $h = 0.8h_{cr}^{iso} = 2.1888\,g_0$, (c) $h = 0.5h_{cr}^{iso} = 1.368\,g_0$, (d) $h = 0.3h_{cr}^{iso} = 0.8208\,g_0$, (e) $h = 0.04h_{cr}^{iso} = 0.10944\,g_0$, and (f) $h = 0$, respectively. Tilt angle ψ is given as 10° and the non-Schmid effects are taken as $\eta_{ss} = 0.08$, $\eta_{mm} = 0$ for all cases.

Fig. 5. Maps of shear rate on slip system 1 at (a) 1%, (b) 2% and (c) 3% engineering strain, respectively; the hardening rate was taken as $h = 0.5 h_{cr}^{iso}$. The non-Schmid effect is given as $\eta_{ss} = 0.08$. The most active slip bands switch positions instead of persisting at the same location as the macroscopic strain increases.

$h = 0.04$, 0.3 and $0.8 h_{cr}^{iso}$. Fig. 6a–c show maps of the lattice rotations, measured in degrees toward the tensile axis from the original $10°$ tilt (positive values show counter-clockwise rotation), at an engineering strain of 3%; the hardening rate was taken as (a) $h = 0.5 h_{cr}^{iso}$, (b) $h = 0.3 h_{cr}^{iso}$, and (c) $h = 0.04 h_{cr}^{iso}$,
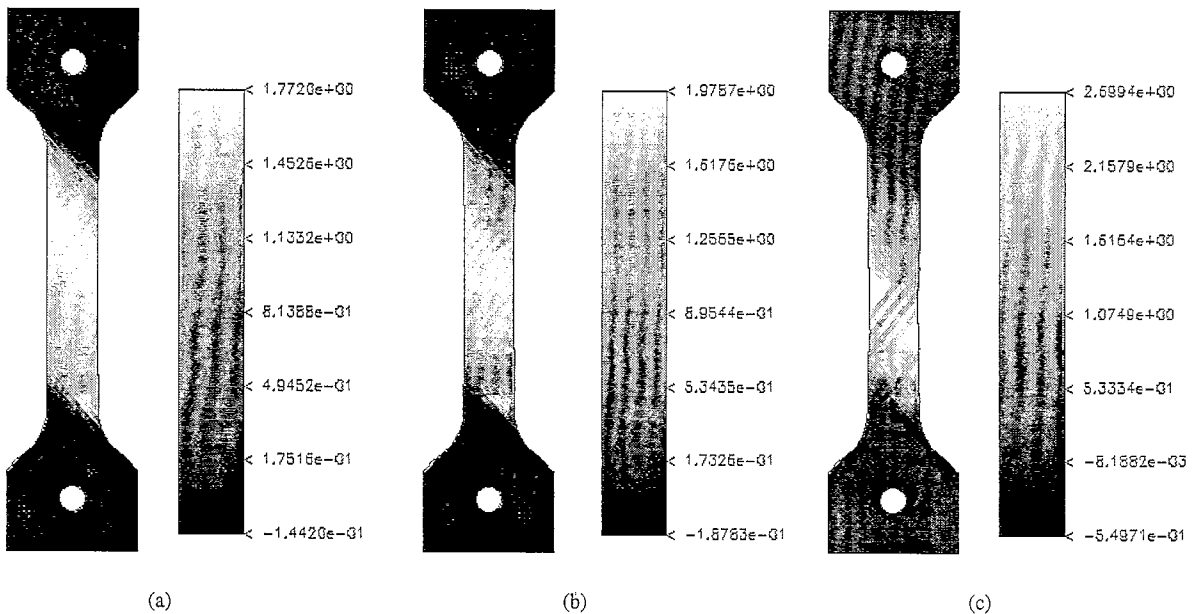
Fig. 6. Map of the lattice rotations, measured in degrees toward the tensile axis from the original $10°$ tilt (positive values show counter-clockwise rotation), at an engineering strain of 3%; the hardening rate was taken as (a) $h = 0.5 h_{cr}^{iso}$, (b) $h = 0.3 h_{cr}^{iso}$, and (c) $h = 0.04 h_{cr}^{iso}$, respectively. The non-Schmid effect is given as $\eta_{ss} = 0.08$.

respectively. It is evident from Fig. 6a–c that (1) the lattice mismatch across the CSB's is finite but very small (less than 1°), and (2) the lattice mismatch across the CSB's increases as the hardening rate goes down. All the shear bands described in these six example simulations were found closely aligned with the active slip system, and the lattice mismatch across the bands is very small.

There is no localization found in cases when $\eta_{ss} = 0$, $\eta_{mm} \neq 0$ or Schmid's rule holds, consistent with bifurcation analyses results. When $\eta_{ss} < 0$ (i.e. $\eta_{ss} = -0.08$), there is no localization either although our bifurcation analyses predicted possible localization, which demonstrated again that bifurcation analyses give only necessary conditions for localization to occur — consistent with discussions given by Dao and Asaro (1993).

3.2.1.2. Serrated flow. Fig. 7 shows stress strain curves for different hardening rates. For $h \leq 0.3 h_{cr}^{iso}$, strong serrated flow is observed, while for $h \geq 0.5 h_{cr}^{iso}$ no serrated flow is observed. Examining the flow curves, one finds that (1) serrated flow can occur at significant hardening rates, i.e. no material softening is necessary, (2) CSB's do not necessarily introduce load drop (serrated flow), only when the hardening rate is low enough, serrated flow will accompany

CSB's, and (3) each serration corresponds to one switch of the most active localization position (or positions), where each switch may involve one to several CSB's shifting to other places. This serration mechanism may be responsible for serrated flows found in many single crystal as well as polycrystal mechanical tests, where material is still under significant hardening.

3.2.1.3. Influences of the non-Schmid effects. We also performed calculations with different non-Schmid factors while keeping other material properties fixed, i.e. using $\eta_{ss} = 0.06$ and 0.04 instead of 0.08. It was found that, as long as there were shear bands forming, (1) the lattice mismatch across the CSB's is finite but very small (less than 1° in our calculations), (2) the lattice mismatch across the CSB's goes up as the non-Schmid factor increases, (3) the peak strains accumulated in those CSB's go higher as the non-Schmid factor increases, and (4) the magnitude of serrated jumps, if there is any, becomes larger as non-Schmid factor increases.

3.2.2. Effect of elastic anisotropy

Our bifurcation analyses (Dao and Asaro, 1996) predicted that elastic anisotropy may play an important role in determining the critical conditions of
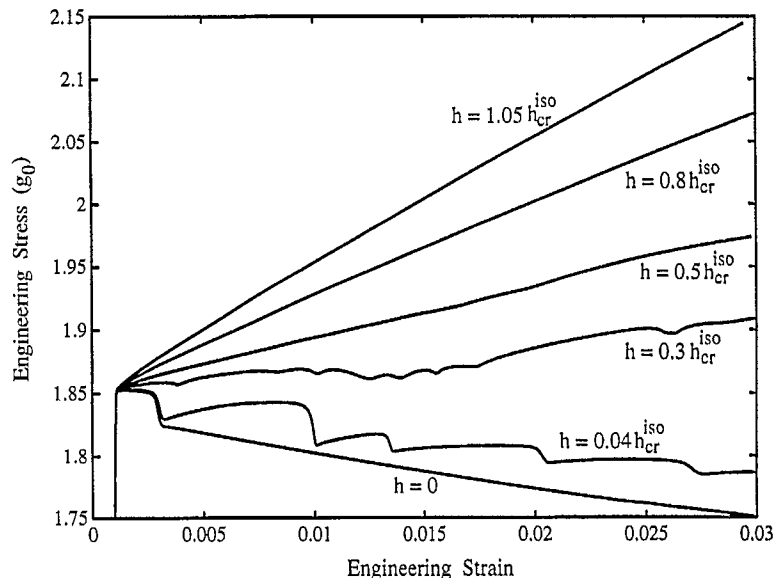

Fig. 7. Stress strain curves for different hardening rates. Noting that, for $h = \leq 0.3 h_{cr}^{iso}$, strong serrated flow is found, while for $h \geq 0.5 h_{cr}^{iso}$ no serrated flow is found. The non-Schmid effect is given as $\eta_{ss} = 0.08$ for all cases.

localization. To verify this, we take elastic constants scaled with Cu single crystals but keep the elasticity constant $C_{44} = G^{iso} = 570 g_0$, i.e. $C_{11} = 1273.05 g_0$, $C_{12} = 917.745 g_0$ and $C_{44} = 570 g_0$. In this case, using the general method presented in Part I (Dao and Asaro, 1996), the critical hardening rate for single slip shear bands is given by

$$h_{cr}^{aniso} = 1.91 g_0,$$

which is 30% lower than for the isotropic case. Two cases will be tested: (a) $h = 1.15 h_{cr}^{aniso} = 0.8 h_{cr}^{iso} = 2.1888 g_0$, and (b) $h = 0.72 h_{cr}^{aniso} = 0.5 h_{cr}^{iso} = 2.1888 g_0$. In case (a), $h_{cr}^{aniso} < h < h_{cr}^{iso}$, thus there should not be any localization for anisotropic elasticity, although if the elasticity is isotropic there is going to CSB's (see Fig. 4b). For case (b), $h < h_{cr}^{aniso} < h_{cr}^{iso}$, there should be localization whether or not the elasticity is isotropic or anisotropic. Fig. 8a, b show maps of the accumulated sum of slips at a 3% engineering strain for cases (a) and (b) respectively; the elasticity was taken as anisotropic. No localization was found in the gage section for case (a) (Fig. 8a), while there were CSB's forming for case (b) (Fig. 8b). If we compare Fig. 4c with Fig. 8b, though the hardening rate was given the same value, the intensity of localization was less and the develop-

ment of CSB's were less complete in Fig. 8b due to the elastic anisotropy.

3.2.3. Summary of single slip results

To summarize, one concludes that both the strain hardening rate and the magnitude of non-Schmid factors are very important in determining whether or not there will be localization, also whether or not there will be CSB patterns or persisting localization, and whether or not there will be serrated flow; a decrease of the strain hardening rate or an increase of the magnitude of the non-Schmid factors can result in an increase of the peak strains accumulated in the CSB's, an increase of the lattice mismatch across the CSB's, and an increase of the serration magnitude if there is a serrated flow; elastic anisotropy influences the critical conditions of localization and the development of the shear bands; and the general method given in Part I (Dao and Asaro, 1996) gives good predictions of critical localization conditions for general anisotropic elastic single crystals.

Bearing in mind that usually the strain hardening is a decreasing function of accumulated shear strain, if CSB's form, clustering and persistence at the same position would be expected at larger strain levels.
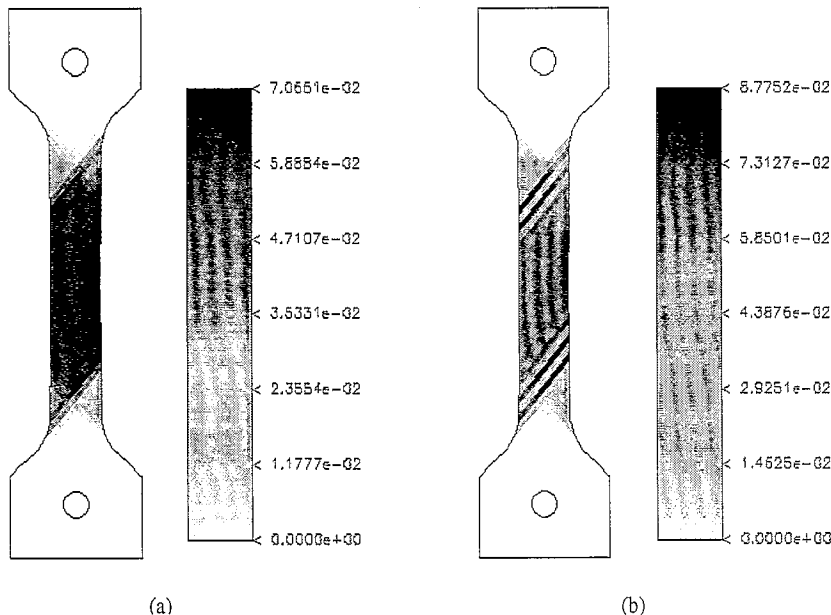

(a)   (b)

Fig. 8. Maps of accumulated sum of slips at 3% engineering strain for (a) $h = 1.15 h_{cr}^{aniso} = 0.8 h_{cr}^{iso} = 2.1888 g_0$, and (b) $h = 0.72 h_{cr}^{aniso} = 0.5 h_{cr}^{iso} = 2.1888 g_0$, respectively; elasticity was taken as anisotropic. The non-Schmid effect is given as $\eta_{ss} = 0.08$.

3.3. Shear bands under multiple slip mode

As studied by Dao and Asaro (1993), non-Schmid effects have important influences on localizations in multiple slip mode. Unlike the single slip shear bands where non-Schmid effects are necessary to introduce localized deformation at positive hardening rates, multiple slip bands can form at positive strain hardening with Schmid's rule. Noting that if $\eta_{ss} = 0.08$, critical hardening rate for single slip shear bands is much higher than that for double slip shear bands, there might be CSB's forming before any multiple slip shear bands present. In this section, Section 3.3, we will focus ourselves on 'pure' multiple slip bands, i.e. $\eta_{ss} = 0$, $\eta_{mm} \neq 0$ or $\eta_{ss} = 0$, $\eta_{mm} = 0$ (Schmid's rule); the cases where there may be possible CSB's to MSB transition will be studied in detail in Section 3.4.

For the multiple slip bands, our analyses about critical conditions of localization (Dao and Asaro, 1996) suggested that, (1) shear bands that oriented close to both primary and conjugate slip systems are possible under positive strain hardening, while 'currently' conjugate slip system is favored; (2) shear bands will be typically several degrees misoriented from the active slip systems and geometrical soften-

ing resulting from non-uniform lattice rotations plays a major role in the initiation and development of the localization; and (3) non-Schmid effects can significantly raise the critical hardening rate of localization. While the bifurcation analyses give us good guidance towards the critical conditions of localized deformation, those predicted conditions are only 'necessary' but not 'sufficient' conditions, therefore finite element methods were used to study non-uniform lattice rotations and different boundary conditions.

3.3.1. Double slip shear bands under symmetric loading

To study localizations under symmetric loading, the slip geometry is given as shown in Fig. 2, with tilt angle $\psi = 0°$ and $\phi = 30°$. When isotropic elasticity is assumed, the elasticity is given the same numbers as for the case in single slip studies, i.e. $G = 570 g_0$ and $\nu = 0.33$. For the calculations presented here, the hardness g is specified by

$$g(\gamma_\alpha) = g_0 + h_\infty \gamma_\alpha + (g_\infty - g_0)$$

$$\times \tanh\left\{ \gamma_\alpha \left(\frac{h_0 - h_\infty}{g_\infty - g_0} \right) \right\},$$

(a)   (b)   (c)   (d)
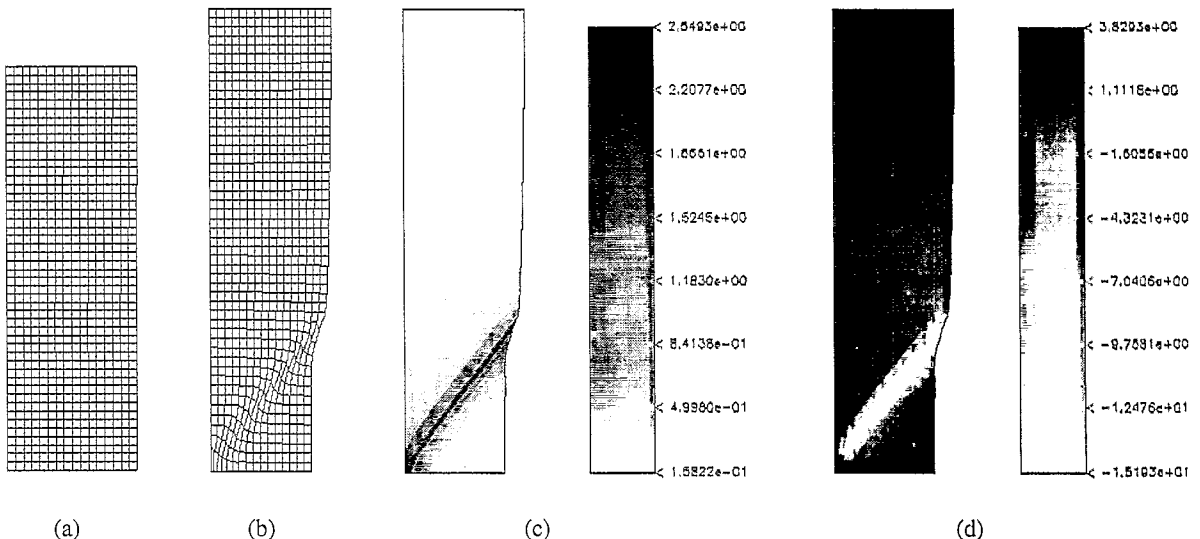
Fig. 9. (a) Original mesh used in double symmetric slip mode of deformation; the aspect ratio b_0/L_0 is given as $1/3$ and the mesh has 16×48 rectangular elements. (b) Deformed finite element mesh, (c) a map of accumulated sum of slips, and (d) a map of lattice rotation measured in degrees (positive values show counter-clockwise rotation), at a engineering strain of 0.15. The non-Schmid effect is given as $\eta_{mm} = 0.08$.

where $g_0 = g(\gamma_\alpha = 0)$, $h_0 = g'(\gamma_\alpha = 0)$, and $h_\infty = g'(\gamma_\alpha = \infty)$, and where the prime denotes differentiation with respect to the indicated argument. In the calculations, we take $g_\infty = 1.8 g_0$, $h_0 = 8.9 g_0$, $h_\infty = 0$. The above mentioned plasticity properties are identical to one of the cases used in Peirce et al. (1982) that proved to be useful for Al–Cu single crystals. Material rate sensitivity exponent m is taken as 0.005 for all cases.

Symmetric conditions are assumed across both the axial and horizontal sections of the crystal and thus the calculations need only be performed on one quadrant of the crystal. The boundary conditions used are:

$$\dot{u}^1 = 0, \dot{T}^2 = 0 \quad \text{on } x^1 = 0, \tag{3.1a}$$

$$\dot{u}^2 = 0, \dot{T}^1 = 0 \quad \text{on } x^2 = 0, \tag{3.1b}$$

$$\dot{T}^1 = \dot{T}^2 = 0 \quad \text{on } x^1 = b_0 + \Delta b_0, \tag{3.1c}$$

$$\dot{u}^2 = \dot{U}, \dot{T}^1 = 0 \quad \text{on } x^2 = L_0. \tag{3.1d}$$

The relations in Eqs. (3.1a) and (3.1b) impose displacement symmetry and shear free traction conditions across the axial and horizontal centerlines, respectively. Traction free conditions are imposed by Eq. (3.1c). Finally, a fixed displacement rate and no shear conditions are imposed on the top boundaries in Eq. (3.1d). The initial geometric imperfection, used to trigger nonuniform deformation, is taken of the form

$$\Delta b_0 = b_0 \left\{ -\bar{\zeta}_1 \cos\left(\frac{\pi x^2}{L_0}\right) + \bar{\zeta}_2 \cos\left(\frac{2\pi x^2}{L_0}\right) \right\}, \tag{3.2}$$

with $\bar{\zeta}_1 = 0.0042$ and $\bar{\zeta}_2 = 0.0024$, in our single slip calculations. The aspect ratio b_0/L_0 is given as $1/3$ and the mesh has 16×48 rectangular elements as shown in Fig. 9a.

3.3.1.1. Cases under Schmid's rule. This type of localization has been studied in detail by Asaro and co-workers (e.g., Asaro, 1979; Peirce et al., 1982; Peirce et al., 1983) Peirce et al. (1983) found that localized deformation patterns are sensitive to latent hardening and material rate sensitivity and geometrical softening plays a very important role. Material

rate sensitivity can delay or even diffuse the localized deformation mode. Strong latent hardening (i.e. $q = 1.4$) can induce patchy slip patterns where only one single slip system is dominating within each 'patch'. The patchy slip and strong latent hardening can give rise to kinematic constrains that prevent shear bands from propagating across the gage completely. Our calculations get the same results as given in Peirce et al. (1983), a detailed description can be obtained from Peirce et al. (1983).

3.3.1.2. Cases with non-Schmid effects. Fig. 9b, c and d show deformed finite element mesh, a map of accumulated sum of slips and a map of lattice rotation measured in degrees (positive values show counter-clockwise rotation), respectively; the deformation is 0.15 engineering strain. The development of macroscopic shearing follows a pattern quite identical to that which occurs within the Schmid description (Fig. 9b and c), and the non-uniform lattice rotations are observed across the shear band (Fig. 9d) which causes geometrical softening to the most active slip system within the band.

For a more quantitative view of the development of shear localization and the influences of the non-Schmid effects, we compare cases where Schmid's rul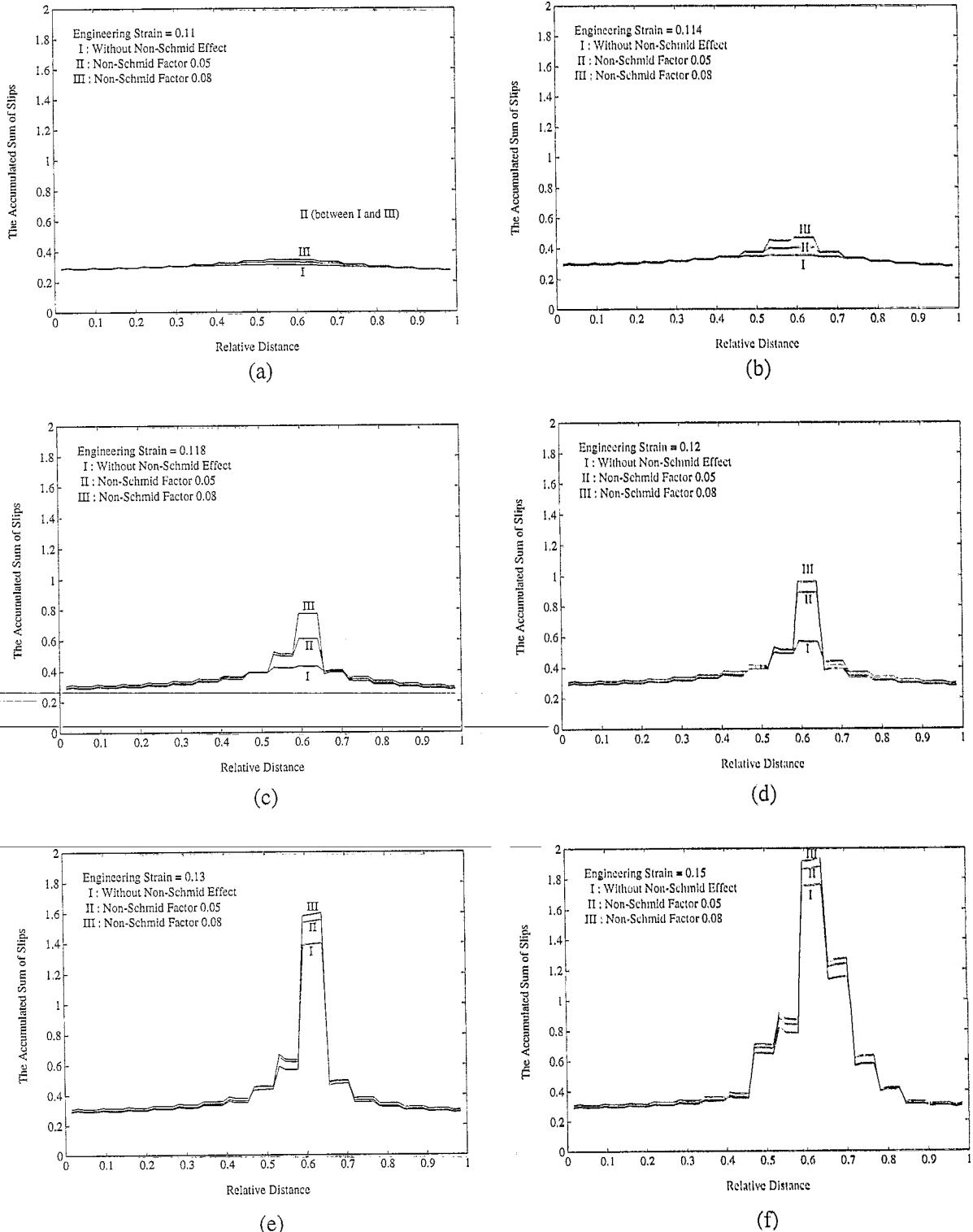e holds and where $\eta_{mm} = 0.05$ and 0.08. Fig. 10a–f illustrate the accumulated sum of slips at distances measured along a row of elements across the shear band location; these six figures correspond to the engineering strains 0.11, 0.114, 0.118, 0.12, 0.13 and 0.15. Fig. 10a–d correspond, evidently, to the strain range in which the localized shearing initiates. The rapid increase in accumulated sum of slips (at a distance of about 0.6) illustrates the initiation of the band, along with the fact that this initiation is abrupt, i.e. it occurs within a very narrow overall macroscopic strain range. Fig. 10e and f correspond to the strain range in which the shear bands fully develop. For the cases with $\eta_{mm} = 0.05$ or 0.08 the localization starts earlier and accelerates before slows down. If we take a look at the map of lattice rotations (Fig. 9d), it is found that the lattice inside the band rotates towards 45° tilt angle. Once the lattice rotation reaches 45°, the effect of geometrical softening saturates, this is why eventually the accumulated sum of slips under Schmid's rule catch up.

Fig. 10. The accumulated sum of slips at distances measured along a row of elements across the shear band location; these six figures correspond to the engineering strains (a) 0.11, (b) 0.114, (c) 0.118, (d) 0.12, (e) 0.13 and (f) 0.15, respectively. Three cases compared are Schmid's rule, $\eta_{mm} = 0.05$, and $\eta_{mm} = 0.08$.

Table 2
Localization patterns under different latent hardening ratios (q) and tilt angles

Latent hardening	Tilt angle (ψ)	Mesh (gage section)	MSB close to
$q = 1.4$	10°	7×21 elements	primary slip plane
	5°	7×19 elements	primary slip plane
$q = 1.0$	10°	7×23 elements	primary slip plane
	5°	7×21 elements	primary slip plane
$q = 0.75$	10°	7×26 elements	primary slip plane
	5°	7×23 elements	conjugate slip plane
$q = 0.5$	10°	7×23 elements	conjugate slip plane
	5°	7×23 elements	conjugate slip plane

The localization process with non-Schmid effects follows a pattern quite similar to that found with Schmid's rule. The bands are observed to form at larger values of h/σ than when Schmid's rule applies, consistent with the rate-independent bifurcation results (Dao and Asaro, 1996). Shear band orientations are also consistent with the general trends found earlier (see for example, Asaro, 1979) in that the bands are characteristically misoriented with respect to the active slip planes. For the crystal model with slip systems oriented symmetrically about the tensile axis the shear bands tend to develop significant misorientations with respect to the slip planes. Misorientations of 5–10° are, in fact, typical.

In all cases, elastic anisotropy has virtually no effect on the localization process, which is consistent with conclusions in Part I (Dao and Asaro, 1996).

3.3.2. Double slip shear bands under non-symmetric loading

To study localizations of this type, the slip geometry is again given as shown in Fig. 2, with tilt angle $\psi = 5°$ or $\psi = 10°$ and $\phi = 30°$. The material properties are given the same as those used in Section

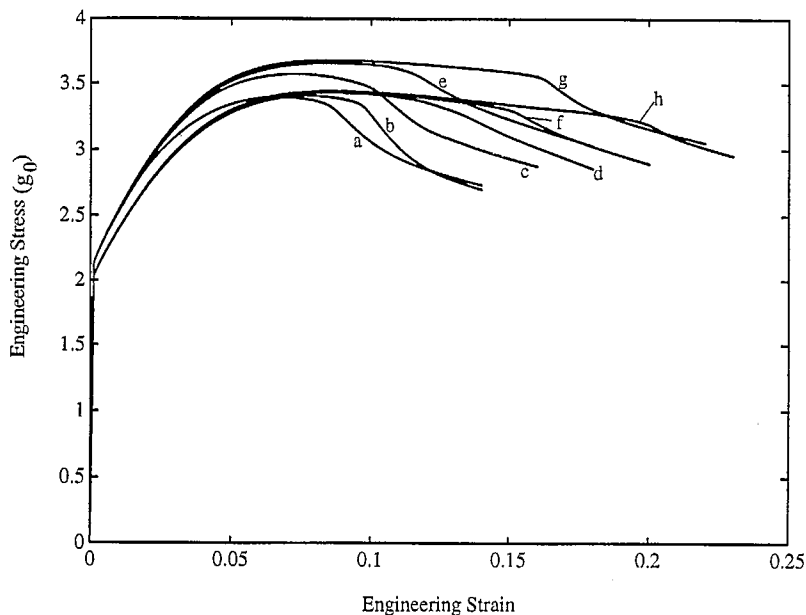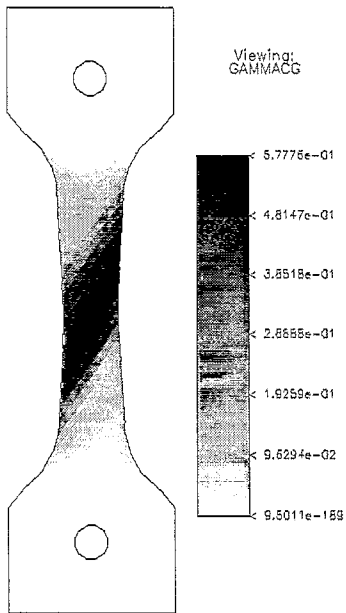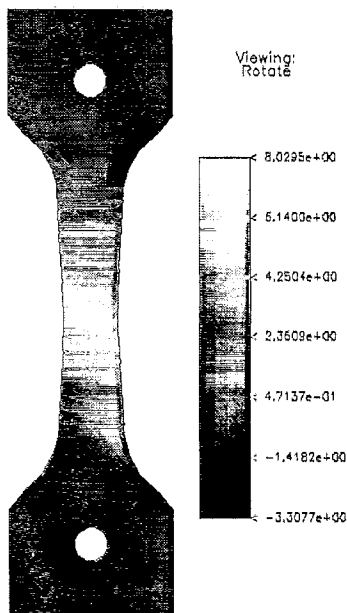Fig. 11. Engineering stress-strain curves for a: $q = 0.5$ and $\psi = 5°$, b: $q = 0.5$ and $\psi = 10°$, c: $q = 0.75$ and $\psi = 5°$, d: $q = 0.75$ and $\psi = 10°$, e: $q = 1$ and $\psi = 5°$, f: $q = 1$ and $\psi = 10°$, g: $q = 1.4$ and $\psi = 5°$, h: $q = 1.4$ and $\psi = 10°$, respectively. Schmid's rule is used for all cases.
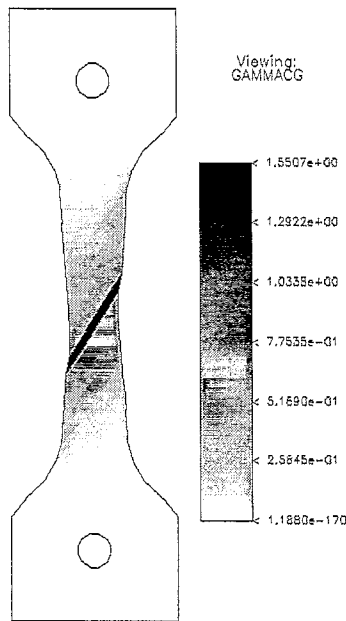
Initial Tilt Angle $\psi = 5^\circ$
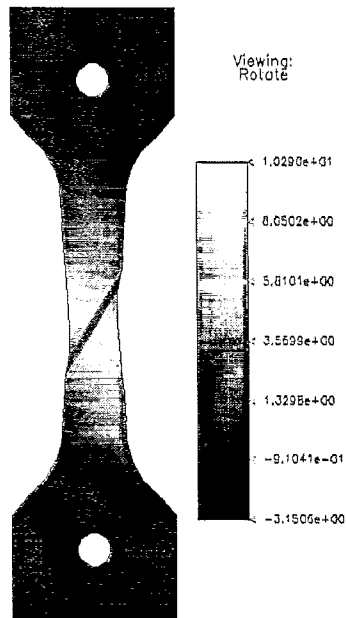Latent Hardening Ratio $q = 1.4$

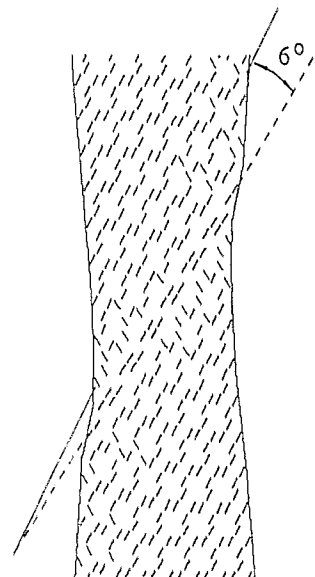(a) γ_a at $\Delta L/L_0 = 0.15$

(b) Lattice Rotation at $\Delta L/L_0 = 0.15$

(c) γ_a at $\Delta L/L_0 = 0.19$

(d) Lattice Rotation at $\Delta L/L_0 = 0.19$

(e) Most Active Slip Direction
at $\Delta L/L_0 = 0.19$

3.3.1. The finite element mesh is built with two grips, similar to that shown in Fig. 3 except that the numbers of elements may be assigned differently for each case. The small initial geometric imperfection taken as $\Delta b_0 = 0.004 b_0 \cos(2\pi x^2/L_0)$, where $b_0/L_0 = 1/3$.

3.3.2.1. Cases under Schmid's rule. A total of eight cases were studied here under different tilt angles and different latent hardening ratios q. Table 2 shows the parameters chosen and localization patterns found for each case studied. Fig. 11 shows engineering stress–strain curves for those eight cases studied. Bearing in mind that bifurcation analyses predicted conjugate slip system is favored while localized shear banding close to both primary and conjugate are possible under significant hardening rate, our results show that some conditions other than those given by the bifurcation analyses are also very important in determining along which direction the shear band is going to form. From observing the stress–strain curves, we notice that usually a MSB corresponds to a sudden drop in its stress–strain curve. Thus it is observed that the strain at which a MSB starts to form gets larger when latent hardening ratio q gets larger or when the tilt angle ψ gets larger. Noting that double slip shear bands can only form under true double slip mode, and since the strain hardening we use here is rather fast saturating (i.e. $h \to 0$ fairly quickly), whether the sample crystal reaches true double slip mode dominates when the localization will occur. Large latent hardening ratio and large tilt angle may both delay the coming of the true double slip mode, and therefore delay the initiation of MSB. In looking at the stress–strain curves, it must be understood that we did not intend to solve stage I to stage II slip transition using our simple latent hardening model, a discussion of this matter can be found in Cuitiño and Ortiz (1993).

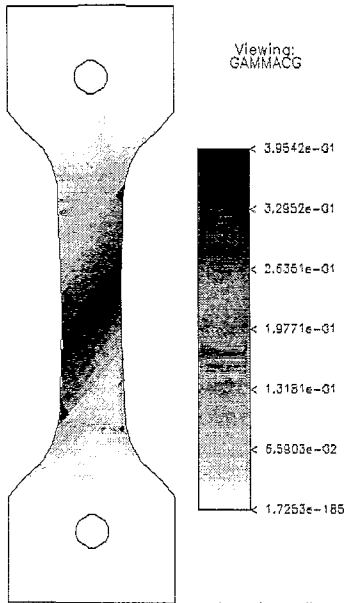To better understand important conditions towards localization other than those necessary conditions predicted by bifurcation analyses, we will look into details of the non-uniform lattice rotations and strain accumulations and their development. Fig. 12 shows the development of the localization process for the case where the latent hardening ratio is taken as $q = 1.4$ and the initial tilt angle is taken as $\psi = 5°$. Fig. 12a and c show maps of accumulated sum of slips at engineering strains of 0.15 and 0.19, respectively; Fig. 12b and d show maps of lattice rotations measured in degrees (positive values show counter-clockwise rotation) at engineering strains of 0.15 and 0.19, respectively; and Fig. 12e shows the current traces of the currently most active slip system in the center of gage section at 0.19 engineering strain.

Fig. 12a–b correspond to an engineering strain of 0.15. The accumulated sum of slips γ_a in Fig. 12a is seen slightly non-uniform at this stage. It is very interesting to observe the overshooting in Fig. 12b in the middle of the gage, noting that rotations above 5° — the initial tilt angle — is overshooting. About 1°–3° overshooting is observed, in agreement with predictions made by Peirce et al. (1983) for $q > 1$. Noting that we have got a conjugate to primary switch here, at least at the middle of the gage section.
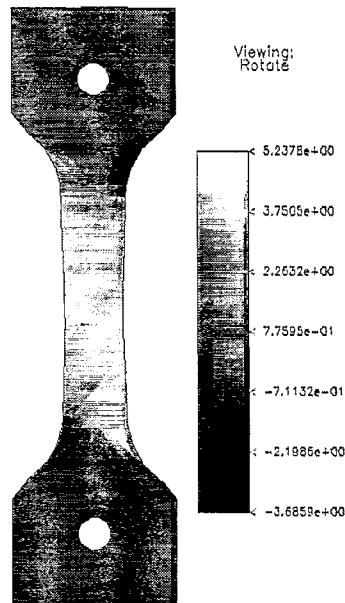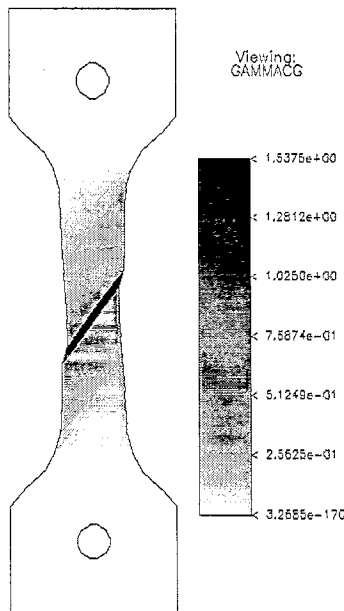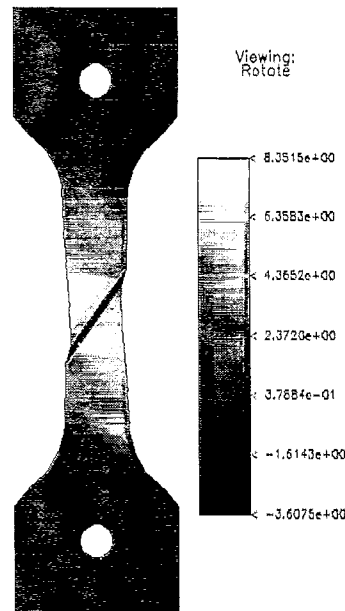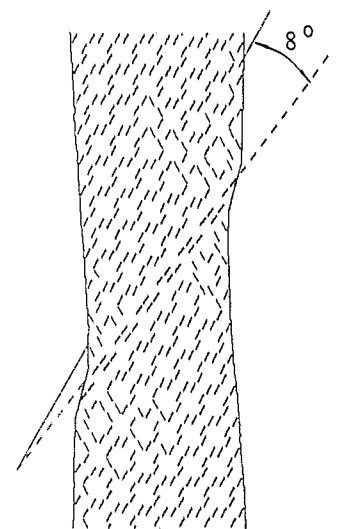
Fig. 12c–d correspond to an engineering strain of 0.19. Unlike the case with symmetric loading conditions where a shear band across the whole gage section is constrained by the 'patches of single slip' for $q = 1.4$ (Peirce et al., 1983), a MSB is well developed under non-symmetric loading here as shown in Fig. 12c. The MSB is found to be close to the original primary slip plane. From Fig. 12d, the map of lattice rotations, it is found that non-uniform lattice rotations and the resulting geometrical softening are again playing an important role here in promoting the localizations. While the gage section rotates counter-clockwise, the lattice inside the shear band rotates much slower than that outside, making the originally primary slip system having the highest shear strain rate. It is noted that the slip system

Fig. 12. Development of the localization process for the case where the latent hardening ratio is taken as $q = 1.4$ and the initial tilt angle is taken as $\psi = 5°$. (a) and (c) show maps of accumulated sum of slips at engineering strains of 0.15 and 0.19, respectively; (b) and (d) show maps of lattice rotations measured in degrees (positive values show counter-clockwise rotation) at engineering strains of 0.11 and 0.15, respectively; and (e) shows the current traces of the currently most active slip system in the center of gage section at 0.15 engineering strain, where some traces of 'bands of secondary slip' are evident.

Initial Tilt Angle $\psi = 5^{\circ}$
Latent Hardening Ratio $q = 1.0$

Viewing:
GAMMACG

< 3.9542e-01
< 3.2952e-01
< 2.6361e-01
< 1.9771e-01
< 1.3181e-01
< 6.5903e-02
< 1.7253e-185

(a) γ_a at $\Delta L/L_0 = 0.11$

Viewing:
Rotate

< 5.2378e+00
< 3.7505e+00
< 2.2632e+00
< 7.7595e-01
< -7.1132e-01
< -2.1985e+00
< -3.6859e+00

(b) Lattice Rotation at $\Delta L/L_0 = 0.11$

Viewing:
GAMMACG

< 1.5375e+00
< 1.2812e+00
< 1.0250e+00
< 7.6874e-01
< 5.1249e-01
< 2.5625e-01
< 3.2685e-170

(c) γ_a at $\Delta L/L_0 = 0.15$

Viewing:
Rotate

< 8.3515e+00
< 6.3583e+00
< 4.3652e+00
< 2.3720e+00
< 3.7884e-01
< -1.6143e+00
< -3.6075e+00

(d) Lattice Rotation at $\Delta L/L_0 = 0.15$

8°

(e) Most Active Slip Direction at $\Delta L/L_0 = 0.15$

hardness (or resistances) of slip system 1 and 2 are not equal at the same 'material point', thus the criterion of geometrical softening should be related directly to the shear strain rate of each slip system instead of only the resolved shear stress! Fig. 12e, the current traces of the currently most active slip system in the center of gage section at 0.19 engineering strain, shows that the lattice inside the shear band is at an angle of about 6° with respect to the surrounding lattice. Some traces of 'bands of secondary slip' are evident.

Fig. 13 shows the development of the localization process for the case where the latent hardening ratio is taken as $q = 1$ and the initial tilt angle is taken as $\psi = 5°$. Fig. 13a and c show maps of accumulated sum of slips at engineering strains of 0.11 and 0.15 respectively; Fig. 13b and d show maps of lattice rotations measured in degrees (positive values show counter-clockwise rotation) at engineering strains of 0.11 and 0.15, respectively; and Fig. 13e shows the current traces of the currently most active slip system in the center of gage section at 0.15 engineering strain.

Fig. 13a–b correspond to an engineering strain of 0.11. The accumulated sum of slips γ_α in Fig. 13a is seen slightly non-uniform at this stage. There is no apparent overshooting found in Fig. 13b in the middle of the gage, noting that only rotations above 5° — the initial tilt angle — is overshooting. This is also in agreement with predictions made by Peirce et al. (1983). Therefore, unlike the case with $q = 1.4$ and $\psi = 5°$, no conjugate to primary switch in this case.

Fig. 13c–e correspond to an engineering strain of 0.15. A MSB is well developed at this stage, see Fig. 13c, and the band direction is close to the primary slip plane. From Fig. 13d, the map of lattice rotations, non-uniform lattice rotations and the resulting geometrical softening again have important influences on the direction of shear band formation. While the gage section rotates counter-clockwisely,

the lattice inside the shear band rotates clockwise (backward), which gives higher resolved shear stress on the primary slip system inside the band. Noting that for this case, the slip system hardness (or resistances) for slip system 1 and 2 are the same for any 'material point' at any instance. Since there is no overshooting at the onset of localization, the primary slip system will have a higher resolved shear stress and higher shear strain rate, and therefore the MSB starts with a direction that is close to the primary slip plane; once the MSB starts forming, the non-uniform lattice rotations result in the resolved shear stress inside the shear band larger than that outside, the shear band will intensify as the deformation gets larger. In Fig. 13e, the current traces of the currently most active slip system in the center of gage section at 0.15 engineering strain, shows that the lattice inside the shear band is at an angle of about 8° with respect to the surrounding lattice. Some traces of 'bands of secondary slip' are evident.

Fig. 14 shows the development the localization process for the case where the latent hardening ratio is taken as $q = 0.75$ and the initial tilt angle is taken as $\psi = 5°$. Fig. 14a and c show maps of accumulated sum of slips at engineering strains of 0.09 and 0.13, respectively; Fig. 14b and d show maps of lattice rotations measured in degrees (positive values show counter-clockwise rotation) at engineering strains of 0.09 and 0.13, respectively; and Fig. 14e shows the current traces of the currently most active slip system in the center of gage section at 0.13 engineering strain.

Fig. 14a–b correspond to an engineering strain of 0.09. The accumulated sum of slips in Fig. 14a is seen slightly non-uniform at this stage. No apparent overshooting can be observed in Fig. 14b in the middle of the gage, noting that only rotations above 5° — the initial tilt angle — is overshooting. Therefore, there is no conjugate to primary switch here.

Fig. 14c–e correspond to an engineering strain of 0.13. A MSB is well developed at this stage (see Fig.

Fig. 13. Development of the localization process for the case where the latent hardening ratio is taken as $q = 1.0$ and the initial tilt angle is taken as $\psi = 5°$. (a) and (c) show maps of accumulated sum of slips at engineering strains of 0.11 and 0.15, respectively; (b) and (d) show maps of lattice rotations measured in degrees (positive values show counter-clockwise rotation) at engineering strains of 0.11 and 0.15, respectively; and (e) shows the current traces of the currently most active slip system in the center of gage section at 0.15 engineering strain, where some traces of 'bands of secondary slip' are evident.

Initial Tilt Angle $\psi = 5^{\circ}$
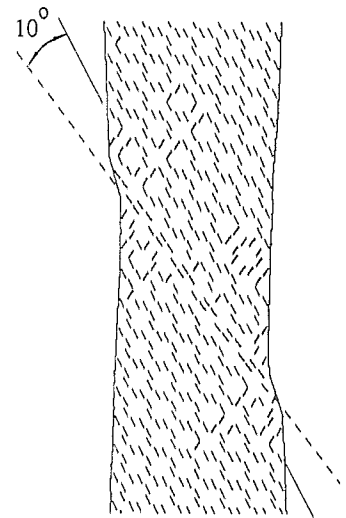Latent Hardening Ratio q = 0.75
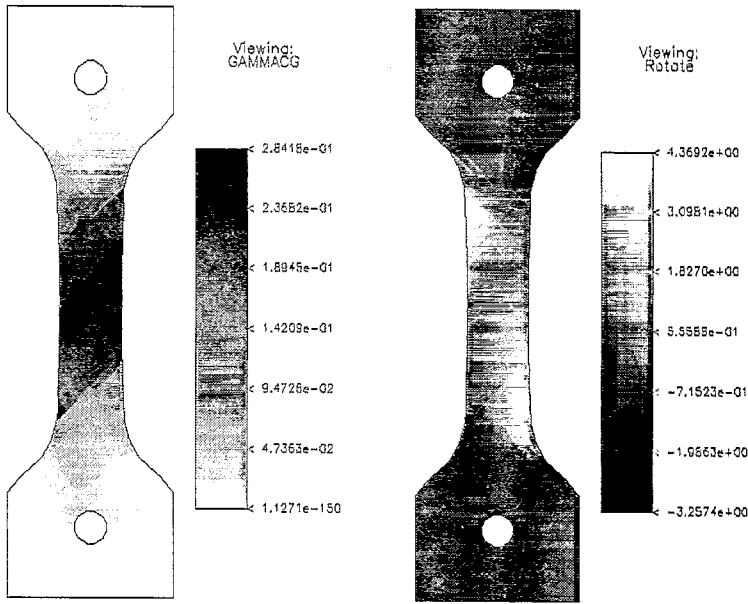
(a) γ_a at $\Delta L/L_0 = 0.09$

(b) Lattice Rotation at $\Delta L/L_0 = 0.09$
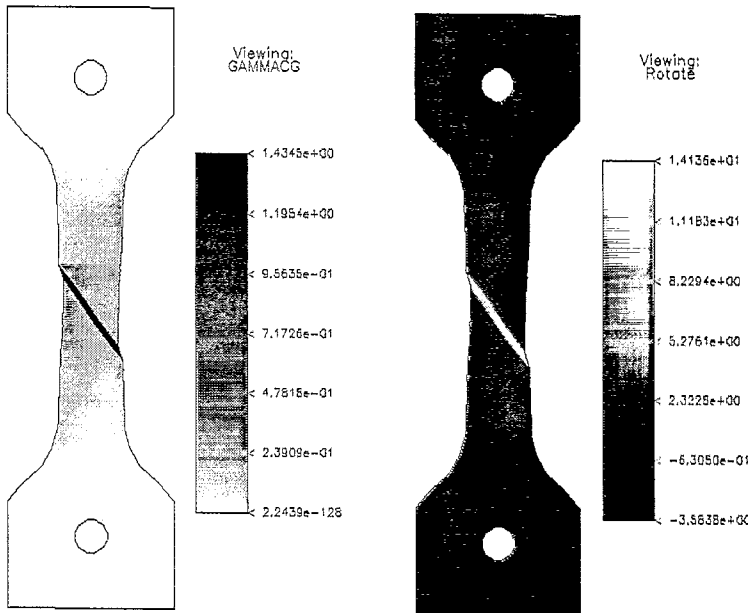
(c) γ_a at $\Delta L/L_0 = 0.13$

(d) Lattice Rotation at $\Delta L/L_0 = 0.13$

(e) Most Active Slip Direction at $\Delta L/L_0 = 0.13$

14c), and the band direction is found to be close to the *conjugate* slip plane. From Fig. 14d, the map of lattice rotations, it may be seen that non-uniform lattice rotations and the resulting geometrical softening again have important influences on the direction of shear band formation. While the gage section rotates clockwisely, the lattice inside the shear band rotates counter-clockwise at a faster rate than the surrounding lattice. Although both slip systems are experiencing higher resolved shear stresses, that on the conjugate slip system becomes larger. Note that for this case, the slip system hardness (or resistances) for slip system 1 and 2 are different at the onset of localization, where the conjugate slip system has the lower hardness since $q = 0.75 < 1$. Thus the conjugate slip system has the higher shear strain rate, and the MSB starts in favor of conjugate slip system. Fig. 14e, the current traces of the currently most active slip system in the center of gage section at 0.13 engineering strain, shows that the lattice inside the shear band is at an angle of about 9° with respect to the surrounding lattice. The domination of the conjugate slip system is clearly seen and some traces of 'bands of secondary slip' are evident.

As we increase the initial tilt angle to 10° and keep the latent hardening ratio $q = 0.75$, we find that the shear band formation follows a pattern very similar to that observed in Fig. 13 where a MSB close to primary slip plane formed. For this case, again there was no overshooting observed before the shear band initiation. What happened was that, although the hardness (or resistance) of the conjugate slip system is smaller than that of the primary slip system at the onset of localization, the rather high initial tilt angle (10°) makes the lattice still highly skewed in favor of the primary slip system, therefore the shear strain rate of the primary slip system is much higher than that of the conjugate which results in localization started at a direction close to the primary slip plane.

3.3.2.2. Cases with non-Schmid effects.

Fig. 15 shows engineering stress–strain curves for Schmid's rule and non-Schmid factor $\eta_{mm} = 0.08$; latent hardening ratio is taken as $q = 1$ and the initial tilt angle $\psi = 5°$. One notices that the sudden load drop, which indicates the initiation of the localization, happens at a later stage for the case with $\eta_{mm} = 0.08$ while our bifurcation results predicted the opposite. This is another perfect example showing that bifurcation results are only the necessary conditions for localization. The localization process is found very similar to that observed in Fig. 13 where a MSB close to primary slip plane formed.

Fig. 16 shows the accumulated sum of slips at distances measured along a row of elements across the shear band location at engineering strains 0.11, 0.13, 0.14 and 0.17, respectively; results under Schmid's rule are in solid lines while results under $\eta_{mm} = 0.08$ are in dashed lines. For the case of $\eta_{mm} = 0.08$, the localization starts slower, and then catches up at higher strains.

The reason why there is a slow initiation and an acceleration process can be understood by studying the lattice rotations involved. The lattice rotations involved are found to be nearly the same for Schmid's rule and $\eta_{ss} = 0.08$ in this case. From Fig. 13b, which illustrates the lattice rotation before shear band formation, the lattice is seen more or less uniformly rotating counter-clockwisely, which results in reduced stress $\tau_{mm}^{(1)}$ (the stress component associated with non-Schmid factor η_{mm} for slip system 1). This kind of lattice rotation will result in continuously increasing τ_{crss}^1 for $\eta_{mm} = 0.08$. while for Schmid's rule τ_{crss}^1 is always a constant. A slow initiation is thus expected for $\eta_{mm} = 0.08$. As the MSB develops further (see Fig. 13d), and the gage section rotates counter-clockwise, the lattice inside the shear band rotates clockwise which leads to a higher Schmid factor for primary slip system and higher values of $\tau_{mm}^{(1)}$. This type of non-uniform

Fig. 14. Development of the localization process for the case where the latent hardening ratio is taken as $q = 0.75$ and the initial tilt angle is taken as $\psi = 5°$. (a) and (c) show maps of accumulated sum of slips at engineering strains of 0.09 and 0.13, respectively; (b) and (d) show maps of lattice rotations measured in degrees (positive values show counter-clockwise rotation) at engineering strains of 0.09 and 0.13, respectively; and (e) shows the current traces of the currently most active slip system in the center of gage section at 0.13 engineering strain, where some traces of 'bands of secondary slip' are evident. The MSB is found to be close to *conjugate* slip plane.
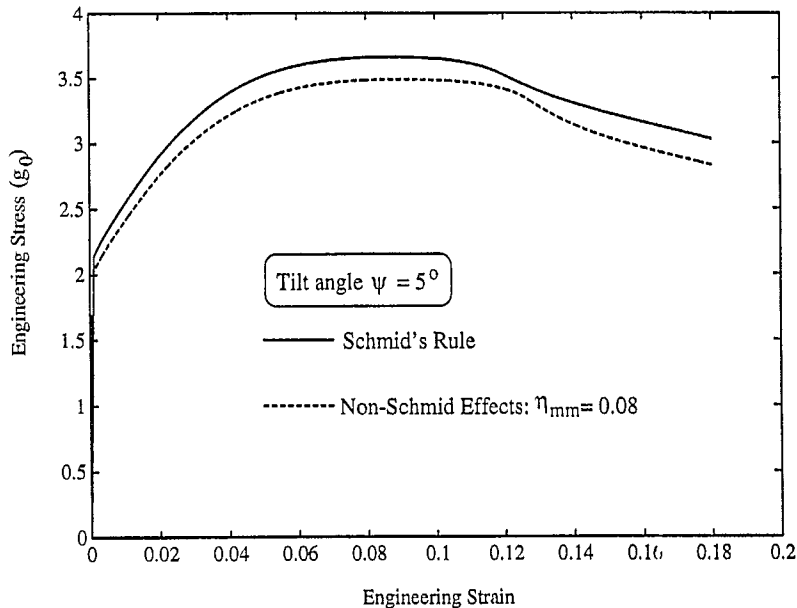
Fig. 15. Engineering stress–strain curves for Schmid's rule and non-Schmid factor $\eta_{mm} = 0.08$; latent hardening ratio is taken as $q = 1$ and the tilt angle $\psi = 5°$.

lattice rotations will result in continuously decreasing $\tau_{crss}^{(1)}$) within the shear band of $\eta_{mm} = 0.08$, while no τ_{crss}^{1} change is expected for Schmid's rule. It is therefore expected that the shear strain rate within

the band should be higher for $\eta_{mm} = 0.08$ than that for Schmid's rule, and this is indeed confirmed by comparing the shear strain rates at 0.15 engineering strain. With higher strain rates within the shear band,
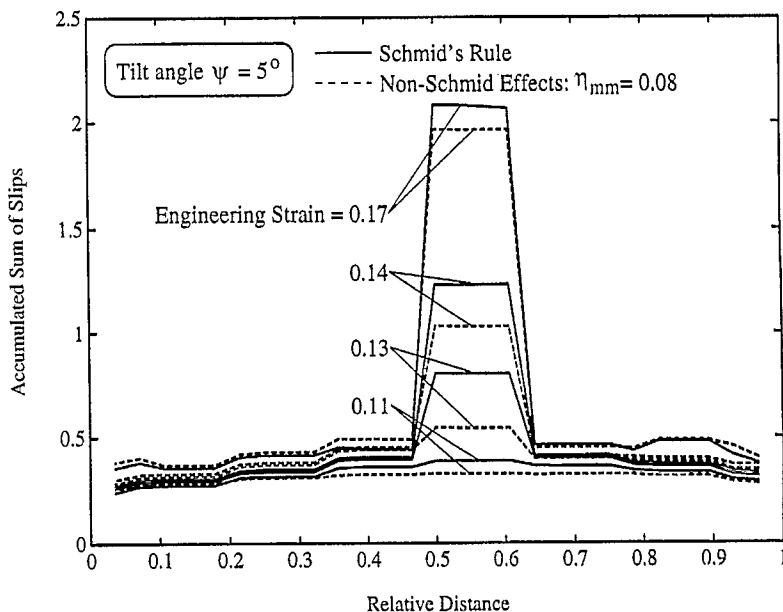

Fig. 16. The accumulated sum of slips at distances measured along a row of elements across the shear band location at engineering strains 0.11, 0.13, 0.14 and 0.17, respectively; results under Schmid's rule are in solid lines while results under $\eta_{mm} = 0.08$ are in dashed lines.

the intensity of the shear band for $\eta_{mm} = 0.08$ will eventually catch up with that for Schmid's rule.

3.4. Coarse slip bands and the transition to macroscopic shear bands

As the bifurcation analyses suggest (see Table 1), for the planar slip geometry used here, the single slip bands are very close to the slip plane (less than 2.3°) while the bands forming under conditions of double slip are 7°–9° misoriented. Another interesting feature is that single slip bands can form at much higher hardening rates than the double slip bands as long as there are modest non-Schmid effects; and if the Schmid rule holds, single slip shear bands are not possible unless there is perfect plasticity or strain softening, while at the same time, double slip shear bands can still form under significant positive strain hardening. From the above analyses, and bearing in mind that hardening rates are generally decreasing functions of strain, we can envision two possible scenarios of shear band formation in single crystals: (1) if Schmid's rule holds, then deformation usually starts in a single slip mode. When the deformation intensifies the lattice rotates so that the conjugate slip system becomes activated, and at the same time, the hardening rate drops with deformation. When the hardening rate drops below the critical hardening rate in double slip, shear bands initiate at an angle which is several degrees misoriented from the active slip systems (whether primary or conjugate depends on latent hardening, tilt angle and boundary conditions); (2) if there are non-Schmid effects, then as the deformation starts in a single slip mode and as the hardening rate drops with deformation, when the hardening rate falls below the critical hardening rate of single slip, single slip shear bands can form on the planes almost parallel to the slip planes. With very high hardening rates the bands will not however, persist at the same location, but instead will tend to be coarsely spread (CSB's). As the conjugate slip system becomes activated and the hardening rate drops below the critical hardening rate of double slip, double slip shear bands initiate at an angle which is several degrees misoriented from the active slip systems (MSB's). Again, whether MSB's will form close to primary or conjugate slip system de-

pends on latent hardening, tilt angle and boundary conditions.

In this section, Section 3.4, the focus is on the above mentioned second possibility where CSB's form before MSB's. We thus taken $\eta_{ss} = 0.08$ as our non-Schmid effects. The elasticity is simply taken to be isotropic and consistent with numbers used in Section 3.3. The plastic properties are given the same as those used in Section 3.3, except latent hardening ratio q may vary.

3.4.1. CSB's to MSB transition: MSB close to primary slip system

To study localization mode of this type, the latent hardening ratio is given as $q = 1$, the tilt angle in Fig. 2 is given as $\phi = 10°$ and the angle $\phi = 30°$. The mesh was built with a grip on each end, the gage section had 19×50 rectangular elements and the initial aspect ratio of the mesh was $1/3$ (width/length). The small initial geometric imperfection, used to trigger nonuniform deformation, was taken of the form $\Delta b_0 = 0.006 b_0 \cos(2\pi x^2 / L_0)$, where b_0 and L_0 are the initial width and length of the gage section, respectively.

Fig. 17 shows the development of CSB's and a MSB for this case. Fig. 17a and c show maps of accumulated sum of slips at engineering strains of 0.09 and 0.15, respectively; and Fig. 17b and d show maps of lattice rotations measured in degrees (positive values show counter-clockwise rotation) at engineering strains of 0.09 and 0.15, respectively.

Fig. 17a and b correspond to an engineering strain of 0.09. CSB's are well developed at this stage, see Fig. 17a, and there is no apparent necking. The CSB's are closely aligned with the primary slip plane. It is also noticed that the deformation mode at this stage is still essentially single slip, i.e. $\dot{\gamma}_1 \gg \dot{\gamma}_2 \approx 0$. In Fig. 17b, lattice mismatch across the CSB's is finite but very small (less than 2°).

Fig. 17c–d correspond to an engineering strain of 0.153. A MSB is well developed at this stage, see Fig. 17c, and the band is close to the primary slip plane. The MSB is found to be misoriented about 5° from the primary slip direction s_1 of the surrounding lattice. The lattice inside the MSB is rotated away from the surrounding lattice by about 5°–7° (Fig. 17d). Necking in the gage section where the MSB forms is apparent. It should be stressed that, if there
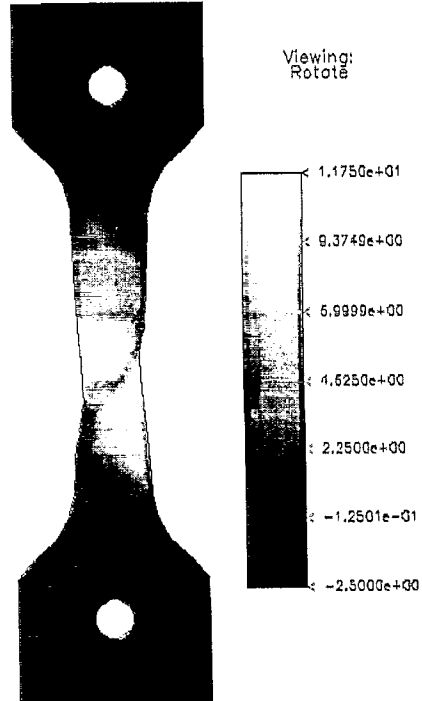
(a) γ_a at $\Delta L/L_O = 0.09$
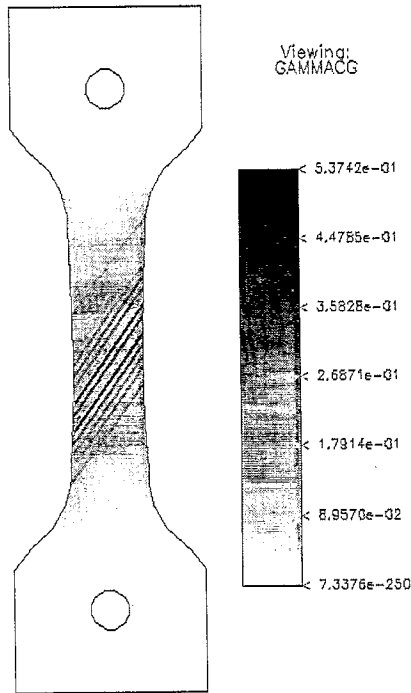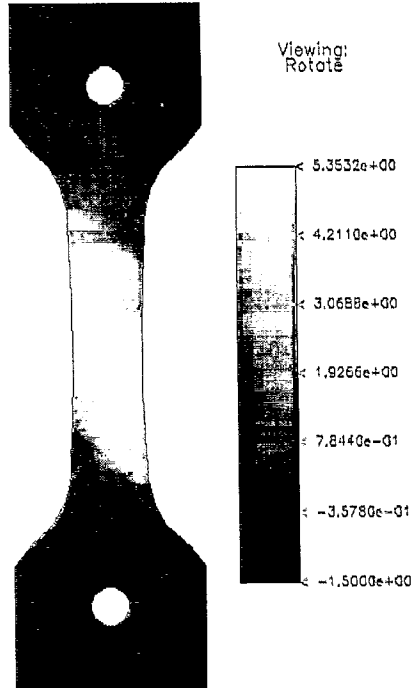
(b) Lattice Rotation at $\Delta L/L_O = 0.09$
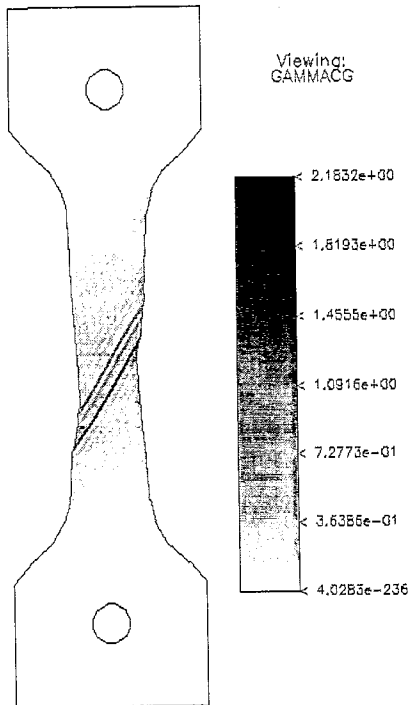
(c) γ_a at $\Delta L/L_O = 0.15$

(d) Lattice Rotation at $\Delta L/L_O = 0.15$

are no non-Schmid effects, there are no CSB's appear in the calculations, although the MSB's form in much the same way as described in the cases discussed in Section 3.3 where there are non-Schmid effects or $\eta_{mm} \neq 0$.

Fig. 18 shows the engineering stress–strain curve, noting that there is serrated flow associated with the CSB's. Since our finite element mesh is not fine enough to catch all the details of CSB formation and serrated flow that goes with it, the band width and the magnitude of serration can not be taken too serious, but this type of calculations shows that non-Schmid effects and the micromechanical processes that induces non-Schmid effects can be the origins of serrated flow.

3.4.2. CSB's to MSB transition: MSB close to conjugate slip system

A example of this type of deformation mode can be found in the case where the latent hardening ratio is given as $q = 0.7$, the tilt angle in Fig. 2 is given as $\phi = 10°$ and the angle $\phi = 30°$. The mesh again was built with a grip on each end, the gage section had 11×49 rectangular elements and the initial aspect ratio of the mesh was $1/5$ (width/length). The small initial geometric imperfection, used to trigger nonuniform deformation, was taken of the form $\Delta b_0 = 0.006 b_0 \cos(2\pi x^2/L_0)$, where b_0 and L_0 are the initial width and length of the gage section, respectively.

Figs. 19 and 20 show the development of CSB's and a MSB for this case. Figs. 19a and 20a show maps of accumulated sum of slips. Fig. 19b, Fig. 20b and Fig. 19c, Fig. 20c show maps of current shear strain rate on the originally primary and conjugate slip systems, respectively. Figs. 19d and 20d show maps of lattice rotations measured in degrees; positive values show counter-clockwise rotation.

Fig. 19 corresponds to an engineering strain of 0.085. From the map of accumulated sum of slips (Fig. 19a), and especially the map of the shear strain rate of the primary slip system (Fig. 19b), the CSB
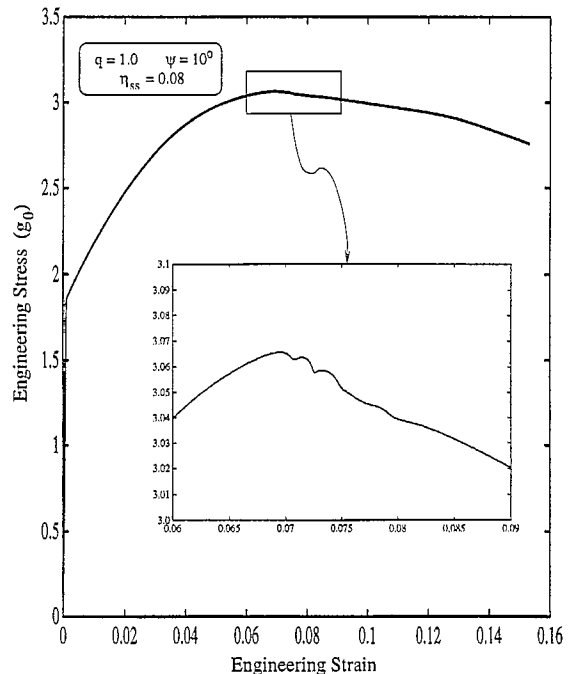

Fig. 18. Engineering stress–strain curve, noting that there is serrated flow associated with the CSB's from the blown up portion. Non-Schmid effects are given as $\eta_{ss} = 0.08$, the latent hardening ratio is taken as $q = 1$ and the tilt angle is taken as $\psi = 10°$.

slip pattern is clear and there is no apparent necking observed. By examining the shear strain rate of the conjugate slip system (Fig. 19c), one can find that the deformation is essentially single slip at this stage, although there is small but finite shearing activity on the conjugate slip system. In Fig. 19d, lattice mismatch across the CSB's is found very small (less than 1°).

Fig. 20 corresponds to an engineering strain of 0.137, where a MSB is well developed along a direction that is very close the conjugate slip direction. Highly concentrated shear can be found from accumulated sum of slips (Fig. 20a) and shear strain rates on both primary and conjugate slip systems (Fig. 20b–c); a double slip mode of deformation is

Fig. 17. Development of CSB's and a MSB for the case where non-Schmid effects are given as $\eta_{ss} = 0.08$, the latent hardening ratio is given as $q = 1$, the tilt angle in Fig. 2 is given as $\psi = 10°$ and the angle $\phi = 30°$. (a) and (c) show maps of accumulated sum of slips at engineering strains of 0.09 and 0.15, respectively; and (b) and (d) show maps of lattice rotations measured in degrees (positive values show counter-clockwise rotation) at engineering strains of 0.09 and 0.15, respectively.

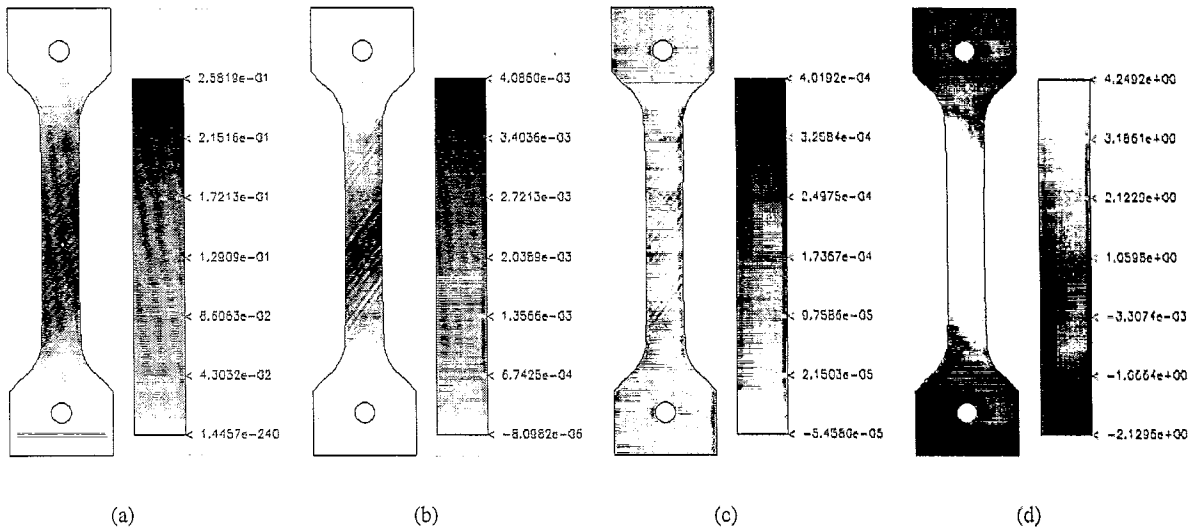(a)   (b)   (c)   (d)

Fig. 19. (a) A map of accumulated sum of slips, (b) a map of current shear strain rate on the primary slip system, (c) a map of current shear strain rate on the conjugate slip system, and (d) a map of lattice rotations measured in degrees (positive values show counter-clockwise rotation), at a engineering strain of 0.085. The non-Schmid effects is given as $\eta_{ss} = 0.08$, the latent hardening ratio is taken as $q = 0.7$ and the tilt angle is taken as $\psi = 10°$.

evident. The MSB is found to be misoriented about 7° from conjugate slip direction s_2 of the surrounding lattice. The lattice inside the MSB is rotated away from the surrounding lattice by about 7°–9° in

the middle and as much as about 15° at the 'necking step' (Fig. 20d).

Fig. 21 shows the engineering stress–strain curve for this case. The abrupt drop indicates the formation

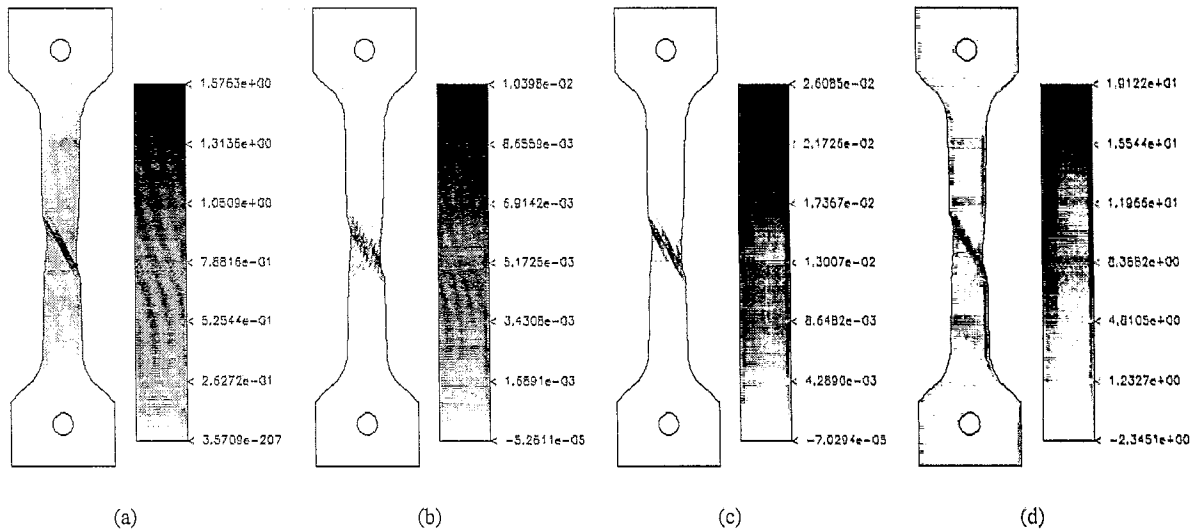(a)   (b)   (c)   (d)

Fig. 20. (a) A map of accumulated sum of slips, (b) a map of current shear strain rate on the primary slip system, (c) a map of current shear strain rate on the conjugate slip system, and (d) a map of lattice rotations measured in degrees (positive values show counter-clockwise rotation), at a engineering strain of 0.137. The non-Schmid effects is given as $\eta_{ss} = 0.08$, the latent hardening ratio is taken as $q = 0.7$ and the tilt angle is taken as $\psi = 10°$.
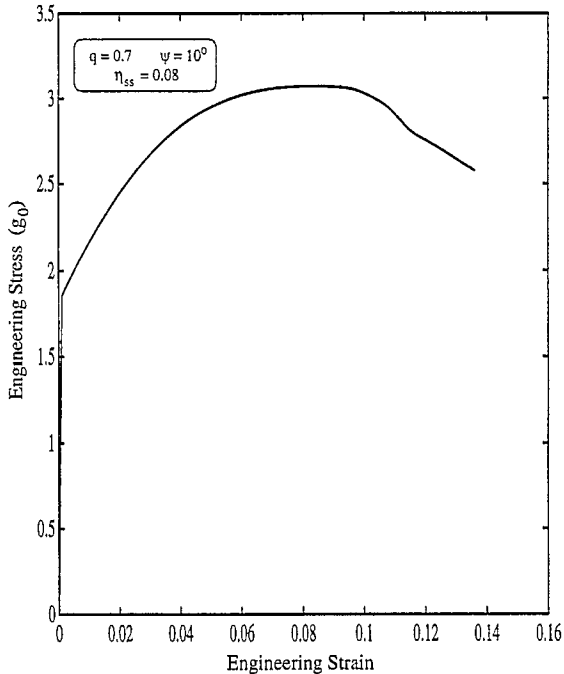
Fig. 21. Engineering stress–strain curve for $\eta_{ss} = 0.08$, $q = 0.7$ and $\psi = 10°$.

of the MSB. There is no apparent serration observed for this calculation. Noting that the CSB's do not have a chance to be well developed (i.e. accumulate a lot of strain) before the MSB takes over, and bearing in mind that the mesh is very coarse for this kind of phenomenon, the serration might be diffused by the mesh; in reality there may still be serrated flow (or load drops) associated CSB formation of this type.

4. Discussion

The results of large scale finite element calculations are consistent with our bifurcation analyses in Part I as well as existing experimental observations. It is again demonstrated that localized deformation can form within defect free, work hardening crystals. Non-Schmid effects, slip system geometry, different loading conditions, and latent hardening are found to be important parameters with respect to the initiation and development of localized deformation.

CSB's can form within crystals undergoing significant hardening and elastic anisotropy has a big influence in terms of the critical conditions of CSB's.

This is the result of the constitutive laws that govern the anisotropic slip geometry and of the deviations from Schmid's rule. Our results of CSB's confirmed the speculation by Price and Kelly that relatively high hardening rate could result in shear bands switching positions after some strain accumulation. It is quite interesting to find that CSB's may be a source of serrated flow. Since CSB's can form under significantly high hardening rates as long as there is moderate non-Schmid effects present, serrated flow can also occur at high hardening rates. It is thus speculated that, CSB slip pattern may be an important source of serrated flow in polycrystalline materials.

MSB's are found to form first on directions that are close to primary slip system as well as conjugate slip system. Non-Schmid effects, latent hardening, and loading geometry (i.e. the orientation of the loading axis with respect to symmetric boundary) are important parameters affecting the initiation and further development of the localization process. Geometrical softening associated with non-uniform lattice rotations is crucial for the development of shear bands. When the single crystal orientation reaches that corresponding to a double slip mode, there may be large differences between the critical resolved shear stresses for the two slip systems, one slip system may have higher resolved shear stress than the other but the shear rate may be lower than the other slip system because the other slip system has a much lower critical resolved shear stress. Accurately accounting for the latent hardening is therefore important. Recently some very encouraging efforts were made along this line, especially with the models developed by Wu et al. (1991), Bassani and Wu (1991) and Cuitiño and Ortiz (1993), where orientation dependent stage I/stage II hardening in copper single crystals can be well captured.

Numerical calculations for transitions from CSB's to a MSB are found consistent with existing experimental observations. It is noted that when Schmid's rule holds (no non-Schmid effects), our calculations did not show any CSB's. This suggests that non-Schmid effects play a very important role in the initiation and development of the localized shear bands.

For simple FCC metals, Schmid's rule is a good approximation. Non-Schmid factors as small as 0.04

(easily unnoticed in experimental verifications of the Schmid rule) can significantly increase the critical hardening rate of localized deformation modes as demonstrated throughout this two part series. Noting that intermetallics may display very high non-Schmid effects, e.g. as observed in Ni_3Al (Umakoshi et al., 1984) and Ni_3Ga (Takeuchi and Kuramoto, 1973), the critical hardening rate of single slip mode is significant, heavy shear banding is observed for those intermetallic compounds at large strains (Gottstein et al., 1989), although very high hardening rates may prevent any significant strain to build up locally, at least at small nominal strains.

Now it is clear that 'secondary' material properties like non-Schmid effects and latent hardening are very important in determining the localized deformation modes. To find the accurate description of those material properties is a great challenge since those parameters are usually coupled together and may evolve with the strain accumulation. Efforts must be joined by micromechanical modeling (i.e. dislocation dynamics), micromechanical testing (i.e. in-situ TEM) as well as carefully designed mechanical tests, continue mechanics modeling and accurate full boundary value numerical computations.

Acknowledgements

References

Asaro, R.J. (1979), Geometrical effects in the inhomogeneous deformation of ductile single crystals, *Acta Metall.* 27, 445.

Asaro, R.J. and J.R. Rice (1977), Strain localization in ductile single crystals, *J. Mech. Phys. Solids* 25, 309.

Bassani, J.L. and T.-Y. Wu (1991), Latent hardening in single crystals – part II. Analytical characterization and predictions, *Proc. R. Soc. Lond. A*, 435, 21.

Chang, Y.W. (1979), An experimental study of shear localization in aluminum–copper single crystals, Ph.D. dissertation, Brown University.

Chang, Y.W. and R.J. Asaro (1981), An experimental study of shear localization in aluminum–copper single crystals, *Acta Metall.* 29, 241.

Cuitiño, A.M. and M. Ortiz (1993), Computational modelling of single crystals, *Modelling Simul. Mater. Sci. Eng.* 1, 225.

Dao, M. and R.J. Asaro (1993), Non-Schmid effects and localized plastic flow in intermetallic alloys, *Mater. Sci. Eng. A*, 170, 1951.

Dao, M. and R.J. Asaro (1994), Coarse slip bands and the transition to macroscopic shear bands, *Scripta Metall.* 30, 791.

Dao, M. and R.J. Asaro (1996), Localized deformation modes and non-Schmid effects in crystalline solids – part I. critical conditions of localization, this issue, Mech. Mater. 23 (1996) 71.

Dao, M., B.J. Lee and R.J. Asaro (1996), Non-Schmid effects on the behavior of polycrystals – with applications to Ni_3Al, *Metall. Trans. A*, 27, 81.

Dève, H.E., S.V. Harren, C. McCullough and R.J. Asaro (1988), Micro and macroscopic aspects of shear band formation in internally nitrided single crystals of Fe–Ti–Mn alloys, *Acta Metall.* 36, 341.

Gottstein, G., P. Nagpal and W. Kim (1989), Recrystallization and texture in boron-doped Ni_3Al, *Mater. Sci. Eng. A*, 108, 165.

Harren, S.V. and R.J. Asaro (1989), Nonuniform deformations in polycrystals and aspects of the validity of the Taylor model, *J. Mech. Phys. Solids* 37, 191.

Harren, S.V., H.E. Dève and R.J. Asaro (1988), Shear band formation in plane strain compression, *Acta Metall.* 36, 2435.

McHugh, P.E., R.J. Asaro and C.F. Shih (1993), Computational modeling of metal matrix composite materials – part I. isothermal deformation patterns in ideal microstructures, *Acta Metall.* 41, 1461.

Peirce, D., R.J. Asaro and A. Needleman (1982), An analysis of nonuniform and localized deformation in ductile single crystals, *Acta Metall.* 30, 1087.

Peirce, D., R.J. Asaro and A. Needleman (1983), Material rate dependence and localized deformation in crystalline solids, *Acta Metall.* 31, 1951.

Price, R.J. and A. Kelly (1964), Deformation of age-hardened aluminum alloy crystals – part II. fracture, *Acta Metall.* 12, 974.

Rashid, M.M. and S. Nemat-Nasser (1990), Modeling very large plastic flows at very large strain rates for large-scale computation, *Comput. Struct.* 37, 119.

Rashid, M.M. and S. Nemat-Nasser (1992), A constitutive algorithm for rate-dependent crystal plasticity, *Comput. Meth. Appl. Mech. Eng.* 94, 201.

Takeuchi, S. and E. Kuramoto (1973), Temperature and orientation dependence of yield stress in Ni_3Ga single crystals, *Acta Metall.*, 21, 415.

Umakoshi, Y., D.P. Pope and V. Vitek (1984), The asymmetry of the flow stress in Ni_3(Al, Ta) single crystals, *Acta Metall.*, 32, 449.

Wu, T-Y., J.L. Bassani and C. Laird (1991), Latent hardening in single crystals – part I. theory and experiments, *Proc. R. Soc. Lond. A*, 435, 1.